First posted online on 18 September 2018 as 10.1242/dev.165688
Access the most recent version at http://dev.biologists.org/lookup/doi/10.1242/dev.165688

Sterols regulate endocytic pathways during flg22-induced defense responses in *Arabidopsis*

Yaning Cui[1,2,*], Xiaojuan Li[1,2,*], Meng Yu[1,2], Ruili Li[1,2], Lusheng Fan[3], Yingfang Zhu[4,5], Jinxing Lin[1,2,‡]

[1]Beijing Advanced Innovation Center for Tree Breeding by Molecular Design, Beijing Forestry University, Beijing 100083, China

[2]College of Biological Sciences & Biotechnology, Beijing Forestry University, Beijing 100083, China

[3]Department of Botany and Plant Sciences, Institute of Integrative Genome Biology, University of California, Riverside, CA 92521, USA

[4]Department of Horticulture and Landscape Architecture, Purdue University, West Lafayette, Indiana 47907, USA

[5]Institute of Plant Stress Biology, State Key Laboratory of Cotton Biology, Department of Biology, Henan University, Jinming Street, Kaifeng 475001, China

[*]Y.C. and X.L. contributed equally to this work.

[‡]Correspondence: Jinxing Lin (linjx@bjfu.edu.cn)

ABSTRACT

The plant transmembrane receptor kinase FLAGELLIN SENSING 2 (FLS2) is critical for innate immunity. Although previous studies have reported FLS2-mediated signal transduction and endocytosis via the clathrin-mediated pathway, whether additional endocytic pathways affect FLS2-mediated defense responses remains unclear. Here, we showed that the *Arabidopsis thaliana* sterol-deficient mutant *steroid methyltransferase 1* displays defects in immune responses induced by the flagellin-derived peptide flg22. Variable-angle total internal reflection fluorescence microscopy (VA-TIRFM) coupled with single-particle tracking showed that the spatiotemporal dynamics of FLS2-GFP changed on the millisecond time scale and the FLS2-GFP dwell time at the plasma membrane increased in cells treated with a sterol-extracting reagent, compared with untreated counterparts. We further demonstrated that flg22-induced FLS2 clustering and endocytosis involves the sterol-associated endocytic pathway, which is distinct from the clathrin-mediated pathway. Moreover, flg22 enhanced the co-localization of FLS2-GFP with the membrane microdomain marker Flot 1-mCherry and FLS2 endocytosis via the sterol-associated pathway. This indicates that plants may respond to pathogen attacks by regulating two different endocytic pathways. Taken together, our results suggest the key role of sterol homeostasis in flg22-induced plant defense responses.

KEY WORDS: Sterols, VA-TIRFM, FLS2, Spatiotemporal dynamics, Endocytosis, Plant immunity

INTRODUCTION

Plants possess a multilayered defense system of innate immunity that confers resistance against many pathogens. Plant cells have a variety of immune receptors, also known as pattern recognition receptors (PRRs), that recognize conserved microbial- or pathogen-associated molecular patterns (PAMPs) (Dodds and Rathjen, 2010; Monaghan and Zipfel, 2012; Felix et al., 1999), such as fungal chitin, and the bacterial factors elongation factor EF-Tu (Kunze et al., 2004), flagellin (Robatzek et al., 2006), and lipopolysaccharides (Mulder et al., 2006; Radutoiu et al., 2007). The *Arabidopsis thaliana* receptor kinase FLAGELLIN SENSING 2 (FLS2) is a well-known PRR that perceives a conserved 22-amino acid domain in the N-terminus of flagellin (flg22) (Mulder et al., 2006; Radutoiu et al., 2007). Upon perception of flg22, FLS2 physically associates with another leucine-rich repeat receptor-like kinase (LRR-RLK), BAK1 (BRASSINOSTEROID-INSENSITIVE 1-ASSOCIATED KINASE 1) (Heese et al., 2007; Roux et al., 2011) and is phosphorylated by BIK1 (BOTRYTIS-INDUCED KINASE 1) (Segonzac and Zipfel, 2011). Activation of FLS2 triggers a series of downstream immune responses (Asai et al., 2002; Boudsocq et al., 2010; Henry et al., 2013) including the production of reactive oxygen species (ROS), induction of defense genes, deposition of secondary compounds such as callose, and accumulation of defense hormones (Grossie et al., 2009; Gomez-Gomez and Boller, 2000; Boudsocq et al., 2010).

Numerous reports support the concept that endocytosis of receptor kinases physically terminates signaling through degradation of receptors, sustains signaling through recycling, or relays signals inside the cell through the formation of signaling endosomes (Du et al., 2013). The recycling/signaling and the degradative fates preferentially associate with different endocytic routes (Sigismund et al., 2008). In animal cells, multiple pathways of endocytosis have been identified and classified, including clathrin-dependent and clathrin-independent pathways (Doherty and McMahon, 2009). Similarly,

two endocytic pathways have been found in plant cells: the clathrin-mediated and sterol/raft-associated endocytic pathways (Fan et al., 2015). The clathrin-mediated endocytic pathway (CME) is the major and best-studied endocytic pathway in plant cells (Ortiz-Morea et al., 2016).

The sterol/raft-associated endocytic pathway has also been described and may involve specific membrane microdomain proteins such as flotillin1 (Flot1) (Li et al., 2012). Membrane microdomains are thought to temporally and spatially organize proteins and lipids into dynamic signaling complexes (Cacas et al., 2012). In animal and yeast cells, sterol-rich domains may function as sorting platforms for proteins that function in signal transduction, pathogen entry, secretion, and endocytosis (Simons and Toomre, 2000). Sterol-associated endocytic pathways have been described in plant cells (Men et al., 2008), although the mechanisms of this pathway in plant immunity have yet to be investigated.

Here, we describe a series of investigations into the mechanism of FLS2 endocytosis, to explore the link between sterols and FLS2 dynamics in response to the plant immunity signal flg22. Phenotypic analyses showed that sterols can affect the flg22-induced immune response. Variable-angle total internal reflection fluorescence microscopy (VA-TIRFM) in combination with single-particle tracking (Li et al., 2011) showed that FLS2 is mobile and heterogeneously distributed at the plasma membrane, and that sterols affect this distribution. Furthermore, we demonstrated that the *sterol methyltransferase 1* (*smt1*) mutation did not change the homo-oligomeric state of FLS2 but did affect FLS2 cluster formation. In addition, endocytosis of FLS2 was impaired in *smt1* mutants. These multifaceted approaches supported the hypothesis that sterol-associated endocytic pathways are essential for the flg22-induced dynamics of FLS2 and plant defense.

RESULTS AND DISCUSSION

The sterol-deficient mutant *smt1* exhibits defects in flg22-induced plant immunity

Plant sterols are key components of membrane microdomains and are connected with defense responses (Kopischke et al., 2013). Interestingly, we found that treatment with the sterol-extracting reagent methyl-β-cyclodextrin (MβCD) increased flg22-induced ROS production (Fig. S1). To further examine the role of sterols in plant immune pathways, we analyzed the flg22-induced immune response in the sterol biosynthesis mutant *sterol methyltransferase 1* (*smt1*) (Diener et al., 2000). SMT1 is a C-24 methyltransferase that catalyzes the first step of sterol biosynthesis, the conversion of cycloartenol to 24-methylenecycloartenolin, and the *smt1* mutant has defects in sterol composition (Diener et al., 2000; Clouse 2002). As shown in Fig. 1 A and B, ROS rapidly accumulated in wild-type plants treated with flg22. However, in the *smt1* mutants, flg22-induced ROS production was significantly higher (up to 40%) compared to the wild type.

To confirm whether the increased ROS production was due to increased expression of *FLS2* in the *smt1* mutants, we performed quantitative reverse transcription PCR (qRT-PCR) to measure *FLS2* expression. We observed no significant difference in *FLS2* mRNA levels between the wild-type and the *smt1* mutant plants (Fig. 1C). Furthermore, immunoblot analysis showed that the FLS2 protein levels were comparable in the wild type and the *smt1* mutant lines (Fig. 1D), indicating that the steady-state levels of the FLS2 receptor likely cannot account for the observed increase in flg22-induced ROS production in the *smt1* mutants, and that sterols affect the flg22-induced ROS burst.

Therefore, we subsequently investigated the role of sterols in flg22-induced plant immunity. By investigating flg22-induced calcium influx, one of the earliest signaling events that occurs within 2-5 minutes after PAMP

perception (Smith et al., 2014), we found that the *smt1* mutants exhibited a rapid and strong increase in $[Ca^{2+}]_{cyt}$ as compared with the wild-type plants (Fig. 1E and 1F), suggesting that, compared with wild type, the *smt1* mutants were more sensitive to the flg22 treatment.

MAP kinases (MAPKs) also play important roles in plant defenses and we next examined flg22-induced MAPK activity in the *smt1* mutants. *CYP81* and *WRKY40* are MAPK-dependent marker genes (Mao et al., 2011; Boudsocq et al., 2010). We found that the increases of *CYP81* and *WRKY40* transcript levels induced by treatment with flg22 were significantly lower in the *smt1* mutants as compared with the wild-type plants at 30 min after treatment (Fig. 1G). We further monitored MAPK activation by measuring MPK phosphorylation in response to flg22 treatment. As shown in Fig. S2, the phosphorylation levels of MPK3, MPK4, and MPK6 were significantly lower in the *smt1* mutants than in wild type, consistent with the qRT-PCR results measuring *CYP81* and *WRKY40* expression (Fig. 1G).

Other studies have examined the effect of brassinosteroids on *smt1* plants (Diener et al, 2000). The root growth of *smt1* mutants is extremely sensitive to epibrassinolide (eBL) treatment (Diener et al, 2000) and eBL can suppress flg22-mediated immunity responses (Belkhadir et al, 2012; Albrecht et al, 2012). However, in *smt1* plants, reduced endogenous brassinolide biosynthesis caused by introducing the brassinosteroid-deficient mutant *deetiolated2* (*det2*) into the *smt1* background did not rescue the poor growth of *smt1* roots (Diener et al, 2000; Carland et al, 2010), suggesting that the phenotypic abnormalities of *smt1* are not due to the accumulation of brassinolides. Therefore, we inferred that the immune defects after flg22 treatment resulted mainly from the altered sterol biosynthesis in *smt1* mutants.

To further investigate the role of sterols in flg22-induced defenses, we examined callose deposition, another important marker of PAMP-mediated immunity. The flg22-induced callose deposition was significantly impaired in the *smt1* mutants as compared with the wild type at 24 hours post-infiltration of

active flg22 (Fig. 1H and Fig. S3), while no difference was detected in the plants infiltrated with H_2O (Fig. 1H and Fig. S3). These analyses of the *smt1* mutants indicate that sterols play a profound role in flg22-induced plant immunity. Consistent with this, accumulating evidence shows that plant immunity is achieved by the formation of nanometer-scale membrane domains (termed microdomains), which act as signaling hubs (Keinath et al. 2010; Stanislas et al. 2009) and sterols are the main lipid components of these membrane microdomains.

FLS2 shows different dynamics at the plasma membrane in the sterol-deficient *smt1* mutants

Membrane-localized receptors sense environmental cues that trigger a physiological response (Li et al., 2013). The flg22 receptor FLS2 is a well-studied leucine-rich repeat receptor in plant immunity, and is used for studies of receptor-mediated immunity in plants (Yeh et al., 2015). Although previous studies have addressed flg22-induced defense responses (Ben Khaled et al., 2015), the dynamic behavior of FLS2 in the plasma membrane remains largely unknown.

Precise analyses with high spatial and temporal accuracy are required to characterize the dynamics of membrane receptors; for example, VA-TIRFM and single-particle tracking of fluorescent proteins can be used to image membrane proteins and measure their dynamic movements. To probe the dynamics of FLS2 in the membrane, we therefore generated transgenic *Arabidopsis* plants expressing *FLS2* fused with *GFP* under the control of the native *FLS2* promoter in the *fls2* mutant. Immunoblot analysis showed that the FLS2-GFP fusion was expressed (Fig. S4A) and *FLS2-GFP* fully rescued the ROS production (Fig. S4B) and callose deposition defects of the *fls2* mutant (Fig. S4C), indicating that FLS2-GFP is functional. We next used VA-TIRFM to image FLS2-GFP in living leaf epidermal cells. The FLS2-GFP fluorescent signal appeared as discrete spots at the plasma membrane (Fig. 2A and 2 B)

and we applied VA-TIRFM to analyze the dynamics of these spots (Wang et al. 2018). We found that numerous FLS2-GFP fluorescent spots disappeared from or came into the focal plane during live-cell imaging (Fig. 2C, D and Movie 1), indicating exocytosis or endocytosis of plasma membrane components. Single-particle tracking analysis of the time series of images revealed that FLS2 is highly mobile and heterogeneously distributed at the plasma membrane.

Sterols are integral components of the cell membrane and affect the lateral mobility of plasma membrane proteins (Saka et al., 2014). To study the effect of sterols on the diffusion of FLS2-GFP, we measured the range of motion of FLS2-GFP in the *smt1* mutants. Under control conditions, the motion range of FLS2 showed a bimodal distribution: long-distance motion (67.8%, 3.05 ± 0.41 μm, the Gaussian peak value) and short-distance motion (32.2%, 1.73 ± 0.13 μm, the Gaussian peak value) (Fig. 2E and 2I). Upon flg22 treatment, the percentage of FLS2-GFP exhibiting short-distance motion decreased to 20.6%, and long-distance motion increased to 79.4% compared to the control (Fig. 2E, I and Movie 2), indicating that flg22 treatment activated long-distance FLS2-GFP movement.

In the *smt1* mutants carrying *FLS2-GFP*, long-distance and short-distance motion accounted for 63.2% and 36.8% (Fig. 2F, I and Movie 3), respectively, indicating that the sterol defect in the mutants slightly affected the range of FLS2-GFP motion. Moreover, under flg22 treatment, the percentage of long-distance and short-distance motion of FLS2-GFP accounted for 73.1% and 26.9% in *smt1* mutants, which was significantly different from the distribution in wild-type Col-0, implying that the *smt1* mutation affects the motion range of flg22-activated FLS2-GFP (Fig. 2F and 2I). This finding was confirmed by treatment with MβCD, which decreased the percentage of long-distance motion of flg22-activated FLS2 (Fig. S5A, B and Movie 4), suggesting that reduction of the amounts of sterols significantly affected the range of motion of flg22-activated FLS2-GFP.

We further plotted the distribution of diffusion coefficients of FLS2-GFP on histograms and fitted the histogram using the Gaussian function, in which we defined the Gaussian peaks (noted as $\hat{G}$) as the characteristic values. In the control, the $\hat{G}$ values were 7.9×10^{-3} $\mu m^2/s$ (SE 7.72 to 8.18 $\times 10^{-3}$ $\mu m^2/s$) (Fig. 2 G and 2 J). In response to the flg22 treatment, the $\hat{G}$ values were 1.48×10^{-2} $\mu m^2/s$ (SE 1.44 to 1.51 $\times 10^{-2}$ $\mu m^2/s$) (Fig. 2G, J and Movie 2), representing a marked increase in diffusion compared to the control plant. To further confirm that the effect was specific to flg22, we used flg22Δ2, a flg22-derived peptide lacking agonist activity (Danna et al., 2011). When the seedlings were treated with flg22Δ2, no significant effect was observed on the range of motion and diffusion coefficients of FLS2-GFP as compared with the control, untreated plant (Fig. 2I and 2 J). In the *smt1* mutants, there was a slight but not significant increase in the diffusion coefficient (from 7.9×10^{-3} $\mu m^2/s$ to 8.85×10^{-3} $\mu m^2/s$) of FLS2-GFP as compared with that in Col-0 without flg22 treatment (Fig. 2H, J and Movie 3). Notably, the diffusion coefficient was 1.07×10^{-2} $\mu m^2/s$ in *smt1* mutants under flg22 treatment, significantly lower than that in Col-0 under flg22 treatment (Fig. 2H and 2 J). A similar result was observed when the plants were treated with MβCD (Fig. S5C, D and Movie 4), supporting the idea that depletion of sterols significantly affects the dynamic behavior of flg22-activated FLS2.

A previous study showed that flg22 perception initiates the innate immune response (Li, et al. 2014). Also, sterol-rich domains may modulate the dynamics and activity of some membrane proteins (Wang et al., 2015; Xue et al., 2018), which are involved in PAMP-induced immunity signaling (Keinath et al., 2010). In the present investigation, we showed that flg22-activated FLS2-GFP spots move faster and diffuse into wider regions in comparison to un-activated FLS2-GFP, indicating that the dynamic behaviors of FLS2 were closely related to flg22-induced signaling. Moreover, disruption of sterols by MβCD treatment or in *smt1* mutants significantly affected flg22-induced plant immunity (Fig. 1) and the diffusion of FLS2-GFP (Fig. 2I and 2 J). Therefore,

we concluded that sterols are involved in the flg22-induced immune responses, acting by regulating FLS2 motions.

Sterols change FLS2-GFP dwell times at the plasma membrane

Previous studies have shown that the binding of signaling molecules to activated receptors resulted in receptor endocytosis (Schlessinger, 2002). Single-particle tracking provides a powerful method to study membrane protein state and local environment, which can constrain protein dwell time (Flores-Otero et al., 2014; Hao et al., 2014). Since flg22-activated FLS2 receptors can internalize into endosomes, we attempted to investigate whether sterols affect the dwell time of FLS2 at the plasma membrane. Therefore, we used VA-TIRFM to investigate the change in dwell time of FLS2 particles in response to flg22 treatment. When the frequency distribution of the FLS2-GFP dwell times under the different treatments was fitted to an exponential function, we found that flg22 treatment led to significantly shorter dwell times (τ = 1.24 s) than that in the control seedlings (τ = 2.15 s) (Fig. 3A–D and 3I). However, MβCD treatment (τ = 2. 73 s) resulted in longer dwell times than that the control seedlings (Fig. 3E, F, and I), while the dwell times of FLS2 became longer in the cells treated with MβCD together with flg22 (τ = 1.91 s) as compared with flg22 treatment (Fig. 3G, H, and I). From the different dwell times of FLS2 at the plasma membrane in the various treatments, we speculated that the internalization of FLS2 into endosomes is a highly efficient way to control FLS2 activity and FLS2 endocytosis may occur through more than one endocytic pathway.

Sterols affect FLS2 clustering rather than changing the homo-oligomeric state of FLS2

The lateral mobility of many membrane receptor proteins depends on their oligomerization status (Low-Nam et al., 2011). Activation of membrane receptor proteins generally involves ligand-induced homo/heterodimerization

or heterooligomerization in membrane microdomains and leads to signal transduction (Schlessinger 2002; Corriden et al. 2014). In a previous study, fluorescence resonance energy transfer (FRET) and bimolecular fluorescence complementation (BiFC) assays showed that FLS2 does not undergo homodimerization either before or after flg22 treatment in *Arabidopsis* protoplasts (Ali et al., 2007), consistent with protein crystal structure studies (Sun et al., 2013). In the present study, by analyzing sequential images, we found that two FLS2 fluorescence spots diffused laterally along the membrane, collided, and then fused together (Fig. 4A). By examining photobleaching steps, which reflect the oligomerization status of the target proteins (Ulbrich and Isacoff, 2007; Das et al., 2007), we found that most of the FLS2-GFP molecules exhibited one-step bleaching, and a few exhibited two-step bleaching (Fig. 4B and 4C) indicating that FLS2 at the plasma membrane of living cells exists in multiple oligomeric forms, including monomers and dimers.

To clarify whether FLS2 exists as dimers, we carried out luciferase complementation assays in *Nicotiana benthaminana* plants, with FLS2-Nluc and the non-interacting protein Cluc-CONSTITUTIVE PATHOGEN RESPONSE 5 (CPR5) as a negative control and FLS2-Cluc plus BIK1-Nluc as a positive control. The results showed that FLS2 can interact with itself and BIK1 but not with CPR5 in the absence or in presence of flg22 (Fig. 4D). To further verify the dimerization of FLS2, we performed co-immunoprecipitation assays in *Arabidopsis* protoplasts. For this purpose, FLS2-HA/FLS2-FLAG and FLS2-HA/BAK1-FLAG were co-transfected into *Arabidopsis* protoplasts. As shown in Figure 4 E, FLS2-HA was detected in the FLS2-FLAG immune complex using anti-HA antibodies both in the absence and presence of flg22 (Fig. 4E), demonstrating that FLS2 can form a homo-dimer either in the inactive or active state.

We next addressed whether FLS2 was predominantly present as a monomer or dimer. Using progressive idealization and filtering (PIF) algorithms, we found that the ratios of the monomer versus the dimer of FLS2-GFP in an

inactive state (0.86:0.14) were similar to the ratios in the active state (0.84:0.16) (Fig. 4F), indicating that monomers are the predominant species. In addition, dimers were detected before and after flg22 treatment. Moreover, with the MβCD treatment, the ratio of the monomer versus the dimer was comparable to that in the control (Fig. 4F), suggesting that sterols do not affect the homo-oligomeric state of FLS2.

Receptor-ligand binding can induce conformational changes of the receptor ectodomain, which result in receptor dimerization and receptor oligomerization or clustering (Clayton et al., 2005). With VA-TIRFM, we observed that most of the FLS2-GFP existed in low-oligomeric spots with an average size of 2.43 × 2.43 ± 0.92 pixels and a fluorescence intensity of 6,968.4 ± 697 counts/pixel in the control plants (Fig. 5A–C). Under flg22 treatment, the FLS2-GFP spots became larger and their fluorescence intensity became brighter as compared with those in the control plant (Fig. 5A). We found that the large spots exhibited exponential decay without discrete steps (Fig. 5D), suggesting that each large spot was a cluster of several FLS2-GFP molecules. The flg22-induced clusters exhibited an average size of 4.12 × 4.12 ± 1.77 pixels and a fluorescence intensity of 12,254.5 ± 1,505 counts/pixel after 30 min (Fig. 5B and C). When treated with MβCD coupled with flg22, the average size and fluorescence intensity of FLS2-GFP spots significantly decreased to 2.83 × 2.83 ± 0.96 pixels and 8,649.5 ± 1,291 counts/pixel (Fig. 5B and C), suggesting that the MβCD treatment resulted in a reduction of flg22-induced FLS2-GFP clusters at the plasma membrane (Fig. S6).

Consistent with previous studies (Gao et al., 2015; Wang et al., 2015), Zipfel and colleagues found that cluster formation relies on the integrity of the plasma membrane, as MβCD-induced sterol depletion of the plasma membrane destroys clustering (Bucherl et al., 2017). Furthermore, clustering is required for kinase activity and abnormal protein complex organization can affect the internalization of membrane proteins (Heus et al., 2013). Therefore, our findings suggest that sterols are involved in modulating FLS2 signal

transduction by adjusting the clustering of FLS2 induced by flg22 at the plasma membrane.

CME only partially inhibited flg22-triggered FLS2 endocytosis

Clustering can promote endocytosis of plasma membrane proteins and this regulates signaling of the receptor (Hofman et al., 2010). FLS2-GFP translocation from the plasma membrane to endosomes is mainly mediated by clathrin (Ben Khaled et al., 2015; Mbengue et al., 2016). We applied fluorescence correlation spectroscopy (FCS) to precisely measure the density of FLS2 molecules under different conditions. FCS is a powerful technique to analyze particle concentrations, mobilities, and diffusion at the single-particle level, and has been successfully applied in plants (Li et al., 2011). Our FCS analyses showed that the density of FLS2 molecules at the plasma membrane significantly increased after treatment with Tyrphostin A23 (TyrA23), which is an inhibitor of the clathrin-mediated endocytosis pathway (Fig. 6A). Similar results were found in equivalent experiments using immunoblot assays (Fig. 6B). In addition, using single particle tracking analysis, we found that the flg22-induced diffusion of FLS2-GFP was significantly impaired in the *clathrin light chain2* (*clc2*) and *clc3* double mutants (*clc2-1 clc3-1*) or using TyrA23 treatment as compared with the control plant (Fig. S7), supporting the notion that clathrin is involved in the internalization of FLS2, as reported previously (Mbengue et al., 2016; Ortiz-Morea et al., 2016).

Moreover, our experiments show that TyrA23 treatment significantly blocked the constitutive endocytosis of FLS2-GFP accumulated in Brefeldin A (BFA) compartments (Fig. 6C), in seedlings treated with BFA. BFA is an inhibitor of vesicle recycling in plants, acting through inhibition of ADP ribosylation factor-guanine exchange factors (Grebe et al., 2003; Naramoto et al., 2014). Quantitative analyses revealed the internalization of flg22-induced FLS2-GFP was not fully blocked (down about 40%) after TyrA23 pretreatment (Fig. 6D and 6E), which was consistent with the results in the *clc2-1 clc3-1*

mutants (Fig. S8). As a control, we analyzed the endocytosis of FLS2-GFP using Tyrphostin A51 (TyrA51), the inactive analog of TyrA23 (Wang et al. 2015) and found that TyrA51 had no significant effects on the internalization of FLS2-GFP (Fig. 6C-E). In addition, we found when co-expressing FLS2-GFP with clathrin light chain (CLC)-mCherry, or with VHA-a-RFP (the *trans-Golgi* network (TGN) markers), FLS2-GFP showed only partial colocalization with CLC-mCherry (17.0%) or VHA-a1-mCherry (14.7%) after 30 min of treatment with flg22 (Fig. 7A). Therefore, these results provided strong evidence that more than one endocytic pathway acts to coordinate the endocytosis of FLS2.

Endocytosis of activated FLS2 is dependent on sterols

Previous reports showed that sterol-enriched domains may play a role in pathogen-associated molecular pattern-induced signaling and affect the endocytosis of plasma membrane proteins in plants (Keinath et al., 2010; Yadeta et al., 2013; Malinsky et al., 2013). In plants, the membrane microdomain-associated endocytic pathway has also been described, and includes microdomain-localized proteins such as flotillins (Li et al., 2012). Yu et al. showed that flg22 can increased the endocytosis of GFP-Flot1 (Yu et al., 2017). Surprisingly, we found that FLS2-GFP showed a significant colocalization with AtFlot1-mCherry (marker of sterol-rich domains) endosomes (44.9%) (Fig.7A). Given the link between membrane microdomains and endocytosis, this finding indicates that sterols may be involved in FLS2 internalization.

To test this hypothesis, we analyzed the degree of colocalization of FLS2-GFP with AtFlot1-mCherry and CLC-mCherry by calculating protein proximity indexes (PPI) (Fig. 7B and C) (Zinchuk et al., 2011). We measured the PPI values before and after flg22 treatment. The results showed that the mean FLS2-to-Flot1 PPI showed a highly significant increase (from 27.2% to 44.8%) in response to flg22. The FLS2-to-CLC PPI also increased significantly (from 48.3% to 60.5%) after 30 min of flg22 treatment (Fig. 7D), confirming that

microdomains are recruited for flg22-dependent FLS2 endosomes.

To test whether sterols affect the internalization of proteins, we applied BFA to inhibit endocytic recycling (Naramoto et al., 2010). FLS2-GFP did not accumulate in BFA compartments in cells treated with MβCD and BFA as compared with BFA alone (Fig. S9). Furthermore, the number of FLS2-GFP endosomes in the *smt1* mutants was notably lower than those in the control after 30 min of flg22 treatment, and this trend became more pronounced after 60 min of flg22 treatment (Fig. 7E and F), which was similar to the results with the MβCD treatment (Fig. S10A and B), indicating the existence of a close relationship between FLS2 localization and sterols. To exclude potential side effects of MβCD, we compensated for the loss of plasma membrane cholesterol by adding MβCD-cholesterol complexes (10 mM) to seedlings following MβCD treatment (Chadda et al, 2007). We found that the internalization of FLS2 recovered after sterol supplementation (Fig. S9 and Fig. S10A, B), indicating the disturbance of FLS2 internalization resulted largely from the depletion of cholesterol, not from potential side effects of MβCD.

Using the relative intensity of cytoplasm/plasma membrane as a proxy for the internalization rate, we found that the ratio in the *smt1* mutants was reduced to 17% after flg22 treatment, which was significantly lower than that in the wild-type plant (27.8%) (Fig. 7G). Similar results were also found in the MβCD pretreated plants (Fig. S10C), suggesting that FLS2 internalization was impaired in the *smt1* mutants.

In the present study, we precisely measured the density of FLS2-GFP on the membrane by FCS. The density of FLS2-GFP on plasma membranes was 11.72 molecules mm^{-2} before flg22 treatment, and 8.93 molecules mm^{-2} after flg22 treatment (Fig. S11A). After treatment with MβCD or MβCD coupled with flg22, the abundance of FLS2 molecules at the plasma membrane significantly changed compared to controls (12.87 molecules mm^{-2} for MβCD and 10.47 molecules mm^{-2} for MβCD coupled with flg22) (Fig. S11A), indicating that the internalization of FLS2-GFP, especially the flg22-induced internalization, was

partly disrupted by MβCD. Western blotting demonstrated that the *smt1* mutation can significantly reduce flg22-induced degradation of FLS2 protein compared with that in the wild type (Fig. 7H), and similar results were obtained under MβCD treatment (Fig. S11B). Sterols are associated with endocytosis (Stanislaset al. 2014, Ferrer A et al. 2017). For example, Hao et al. revealed that sterol extraction by treatment with MβCD significantly disrupted NaCl-induced GFP-RbohD internalization (Hao et al. 2014). Furthermore, the sterol biosynthesis mutants *cyclopropylsterol isomerase1-1* (*cpi1-1*) and *sterol methyltransferase 1* (*smt1*) impaired endocytosis of PIN2 protein (Men et al., 2008; Willemsen et al., 2008). Taken together, these results further support the hypothesis that sterols coordinate the internalization of FLS2.

Endocytosis plays key roles in regulating signaling initiation at the plasma membrane, where plants can sense the external stimuli and signaling through cell surface receptor-like kinases (RLKs) (Barbieri et al. 2016). Some RLKs (including BRI1, FLS2, EFR, and PEPR1/2) have been reported to undertake receptor-mediated endocytosis following ligand perception (Irani et al., 2012; Mbengue et al., 2016; Ortiz-Morea et al., 2011). More importantly, several lines of evidence support the idea that the sterol-associated endocytosis is involved in RLK stability and endocytosis. For instance, sterols are essential for the activation of BRI1 signaling and BRI1 internalization (Wang et al., 2015). Given that sterols are involved in the internalization and signal transduction of FLS2 after sensing flg22, we speculated that sterols exert a profound role in regulating RLK endocytosis, which controls receptor availability on the plasma membrane and fine tunes the delivery of signals to diverse downstream effectors, ultimately regulating the cellular response to different types of signals.

MATERIALS AND METHODS

Plant Materials

All mutants and transgenic lines used were in the *Arabidopsis thaliana* Col-0 background. *Arabidopsis* seeds were surface-sterilized for 30 sec in 85% EtOH/H_2O_2 and vernalized at 4°C for 1 day in the dark. Seedlings were then grown on half-strength Murashige and Skoog (MS) medium. The plants were grown at 22°C under fluorescent light at 70% relative humidity with 16-h-light/8-h-dark photoperiods, unless otherwise specified. The following mutant and transgenic *Arabidopsis* lines have been described previously: *fls2*, *smt1*, *clc2-1clc3-1*, clathrin light chain (CLC)-mCherry, Flot 1-mCherry, VHA-a1-RFP (Gomez-Gomez and Boller, 2000; Diener et al., 2000; Wang et al., 2013; Li et al., 2012; Li et al., 2012; Mbengue et al., 2016). Dual-color lines expressing FLS2-GFP with CLC-mCherry, Flot1-mCherry, and VHA-a-RFP were generated by crossing.

Constructs

To generate the *FLS2* transgenic plants, a native *FLS2* promoter of 988 bp in length and the *FLS2* gene double myc-tag fusion were PCR amplified and cloned into pCAMBIA2300. The *FLS2* promoter sequence was PCR amplified using the primers 5'-GGAATTCGAAGTTGTGAATTGTGATCATAGGA-3' (forward) and 5'-GGGGTACCGGTTTAGACTTTAGAAGAGTT-3' (reverse) carrying the *Eco*RI and *Kpn*I sites. The coding sequence for *FLS2* (At5g46330) was PCR amplified using the primers 5'-GGGGTACCATGAAGTTACTCTCAAAGACCTTTTTG-3' (forward) and 5'-ACGCGTCGACAACTTCTCGATCCTCGTTACGATCT-3' (reverse) carrying the *Kpn1* and *Sal1* sites. The *FLS2* promoter and *FLS2* constructs were constructed by PCR-based cloning in vector pCAMBIA2300. Desired *pFLS2:FLS2-2×myc-GFP* plasmids were introduced into the *fls2* mutant plants by *Agrobacterium*-mediated transformation.

Drug Treatments

All chemicals were purchased from Sigma-Aldrich, if not otherwise indicated, and used at the following concentrations: TyrA23 (50 mM in DMSO, working solution 50 µM), TyrA51 (50 mM in DMSO, working solution 50 µM), Methyl-β-cyclodextrin (MβCD) (200 mM in water, working solution 10 mM), Brefeldin A (BFA) (50 mM in DMSO, working solution 50 µM), FM4-64 (5 mM in DMSO, working solution 5 µM). The flagellin peptides flg22 and flg22Δ2 were synthesized by GL Biochem (Shanghai) Ltd. and were used in a concentration of 10 µM (10 mM in ddH_2O). The TyrA23, TyrA51, MβCD, and BFA treatments were performed as described (Wang et al. 2015) and stock solutions were diluted with 1/2 MS growth medium.

Microscopy

Arabidopsis seedlings were imaged with an Olympus FluoView 1000 inverted confocal microscope fitted with a 60x water-immersion objective (numerical aperture 1). GFP/FM4-64 and RFP/mCherry were excited with 488 and 561 nm wavelengths, respectively, and the fluorescence emission spectra were detected at 500–530 nm for GFP, 600–700 nm for FM4-64, and 580–620 nm for RFP/mCherry. The original images were obtained from the same confocal microscope with the same laser and camera settings and then images were processed using the Olympus, Adobe Photoshop CS5, and the Image J software packages.

TIRFM and Single-Particle Fluorescence Image Analysis

Total internal reflection fluorescence microscopy (TIRFM) was performed on an inverted microscope with a total internal reflective fluorescence illuminator and a 100× oil-immersion objective (Olympus; numerical aperture = 1.45). For the detection of FLS2-GFP particles at the plasma membrane, living leaf epidermal cells of 5-day-old seedlings were observed under VA-TIRFM. The images were acquired with 100 ms exposure times and time-lapse series

images of single particles of FLS2-GFP were taken at up to 100 images per sequence. Proteins labeled with GFP or mCherry were excited with 473-nm or 561-nm laser lines, respectively, from a diode laser (Changchun New Industries Optoelectronics Tech. Co., Changchun, China) and their emission fluorescence was obtained with a filter (BA510IF for EGFP; HQ605/52 for mRFP). The fluorescent signals were acquired by a digital EMCCD camera (ANDOR iXon DV8897D-CS0-VP, Andor Technology, Belfast, UK) after filtering with two band-pass filters (525/545 and 609/654 nm). Images were acquired with 100 ms exposure times and stored directly on a computer. The methods used to analyze single-particle tracking were described previously (Wang et al. 2015).

A program named “progressive idealization and filtering” (PIF) was used for the photobleaching step analysis. After background subtraction by the rolling ball method in Image J software, images were input into the PIF program and subjected to the steps described previously (McGuire et al., 2012).

FCS Analysis

FCS was carried out on a Leica TCS SP5 FCS microscope equipped with a 488-nm argon laser, an in-house coupled correlator, and an Avalanche photodiode. After acquiring images of cells in transmitted light mode, FCS was performed in the point-scanning mode. The diffusion of FLS2-GFP molecules into and out of the focal volume changed the local concentration of the fluorophore number, which led to spontaneous fluctuation of the fluorescence intensity. Finally, the FLS2-GFP density of individual cell membranes was calculated according to the protocol described previously (Li et al., 2011). Up to six random points were selected in one cell, five cells were chosen from a leaf, and at least three representative leaves were measured for each study.

Quantification of Cytoplasm and Plasma Membrane Fluorescence

The images were obtained with a FluoView 1000 laser-scanning microscope (Olympus). The relative surface of the internalized proteins or relative fluorescence intensity at the plasma membrane was calculated with Image J software (National Institutes of Health, version 1.48) as previously described (Du et al., 2013).

Western Blotting

Total proteins were extracted from 10-day-old seedlings of transgenic *FLS2-GFP* lines in the *fls2* or *smt1* mutant backgrounds under different conditions. The GFP antibody (Sigma) was raised against GFP peptides of FLS2-GFP protein. FLS2-GFP protein was denatured in buffer E (100 ml buffer E includes 1.5125 g Tris-HCl [pH 8.8], 11.1 ml glycerine, 1.2409 g $Na_2S_2O_5$, 5 mM DTT, and 1 g SDS). Proteins were separated with an 8% SDS-polyacrylamide gel and transferred to a nitrocellulose membrane. A 1:4,000 dilution was used for the anti-GFP antibody.

Measurement of Net Flux of Ca^{2+}

The net flux of Ca^{2+} was measured using the non-invasive micro-test technique (NMT) method, as previously described (Yan et al., 2015). This technique is used to study the flux of specific molecules from single cells and/or tissues, and is also known as the self-referencing microelectrode technique. The Ca^{2+} electrode was fabricated as described by Yan (Yan et al. 2015). Pre-pulled and silanized glass micropipettes (2-4 μm aperture) were first filled with a backfilling solution (Ca^{2+}: 100 mM $CaCl_2$) to a length of about 1 cm from the tip. Then, the micropipettes were front-filled with selective liquid ion exchange (LIX) cocktails to a column length of approximately 25 μm. The LIX cocktails were obtained from Sigma-Aldrich (Sun et al., 2009). An Ag/AgClelectrode holder was inserted from the back of the electrode until the tip contacted the surface of the electrolyte solution. DRIREF-2 (World

Precision Instruments) was used as a reference electrode. The electrodes were calibrated prior to the experiment in known calibration solutions (0.05, 0.1, and 0.5 mM Ca^{2+}). Only electrodes with Nernstian slopes between 53 and 62 mV/[log-C(±z)] were used in our study (where z is the valence of the ion and C is the concentration of the ion).

Leaves from seven-day-old seedling leaves were fixed on the bottom of a 35-mm dish incubated in the test buffer. Then, the Ca^{2+} flux of the leaves was measured using NMT. Each plant was measured once. The leaves were then treated with 0.1 μM flg22 and the Ca^{2+} flux was measured again. The final flux values were reported as the mean of 7 to 11 individual leaves. The Ca^{2+} fluxes were calculated as described by Yan (Yan et al., 2015).

Quantitative Reverse-transcription PCR

Total RNA was extracted from 10-day-old seedlings with a TiangenNApre Plant Kit (Tian gen) according to the manufacturer's instructions. Reverse transcription was performed using FastQuant RT Kit (Tian gen). qPCR was performed with the TiangenSurperRealPreMix Plus (SYBR Green). The flg22-induced early-response genes and primers were listed as follows: *WRKY40* (*At1g80840*), 5'-GATCCACCGACAAGTGCTTT-3' and 5'-AGGGCTGATTTGATCCCTCT-3'; *CYP81f2* (*At5g57220*), 5'-CTCATGCTCAGTATGATGC-3' and 5'-CTCCAATCTTCTCGTCTATC-3'.

Detection of Callose Deposition

Detection of callose deposition was performed as previously described (Cao et al. 2013). In brief, 7-day-old seedlings were infiltrated with 2 μM flg22 in 6-well plates for 24 hours. Control treatments were infiltrated with H_2O. Excised leaves were immediately cleared in 95% ethanol:H_2O (3:1) for at least 6 hours. Subsequently, samples were rinsed with 50% ethanol and H_2O. Seedlings were stained with aniline blue in 0.15 M phosphate buffer (pH = 9.5) and callose deposits were visualized using ultraviolet epifluorescence microscopy

as described previously (Cao et al., 2013).

Oxidative Burst Measurement

ROS burst experiments were performed by a luminol-based assay as described previously (Sun et al., 2012). Leaves of 4-week-old transgenic *Arabidopsis* plants were sliced into 1-mm strips and incubated in 100 µL of H_2O in a 96-well plate overnight. Then, the H_2O was replaced by 100 µL of reaction solution containing 50 µM of luminol and 10 µg/ml of horseradish peroxidase (Sigma) supplemented with 100 nM of flg22. Luminescence was acquired over time using a Photek camera and software. The reported data are pooled measurements from six independent leaves per condition originating from a minimum of three plants.

Co-Immunoprecipitation Assay

Protoplasts were isolated and transfected as previously described (Niu and Sheen, 2012). After incubation overnight, transformed protoplasts were treated with water or 1 mM flg22 for 10 min. Total protein was extracted with protein extraction buffer (50 mM HEPES [pH 7.5], 150 mM KCl, 1 mM EDTA, 0.2% Triton X-100, 1 mM DTT, proteinase inhibitor cocktail (Roche)). For anti-FLAG IP, total protein was incubated with 50 µL agarose-conjugated anti-FLAG antibody (Sigma) for 4 h. After washing 6 times with extraction buffer. The bound protein was eluted by incubating with 3× FLAG peptide (Sigma) for 1 h. The immunoprecipitates were separated by SDS-PAGE and detected with immunoblotting.

Data Analysis

The significance of arithmetic mean values for all data sets was assessed by Student's *t*-test. Error bars were calculated with the STDEV function in Microsoft Excel. The differences at $P<0.05$ were considered statistically significant. According to Student's *t*-test, characters in the figure represent statistically significant differences compared with control (*$P < 0.05$, **$P < 0.01$

and ***P < 0.001).

Accession Numbers

Sequence data from this article can be found in the *Arabidopsis* Information Resource (TAIR) database under the following accession numbers: *FLS2* (AT5G46330), *Flot 1* (AT5G25250), *smt1* (At5g13710).

Acknowledgments

We sincerely thank Dingzhong Tang (University of Chinese Academy of Sciences) for providing the *fls2* mutant line and Timothy Nelson (Yale University) for providing the *smt1* mutant line. We also thank Qihua He (Peking University) for technical assistance with FCS.

Competing interests

The authors declare no competing or financial interests

Author contributions

Y.C., X.L., M.Y., and J.L. designed research; Y.C., X.L., and M.Y. performed research; R.L., L.F., and Y.Z. contributed new reagents/analytic tools; Y.C., X.L., analyzed the data, Y.C., X.L., M.Y., and J.L. wrote the paper.

Funding

This work is supported by the National Natural Science Foundation of China (31530084, 31622005, 31670182), Beijing Advanced Innovation Center for Tree Breeding by Molecular Design, the Program of Introducing Talents of Discipline to Universities (111 project, B13007).

Supplemental information

Fig. S1. MβCD affected flg22-induced ROS production.

Fig. S2. Detection of the MAPKs phosphorylation in *Arabidopsis thaliana.*

Fig. S3. Flg22 induced callose deposition.

Fig. S4. Rescue of the *fls2* mutant by a genomic sequence of *FLS2* fused with

the *GFP* sequence in *Arabidopsis* leaves.

Fig. S5. Effects of MβCD treatment on the dynamic behavior of FLS2-GFP.

Fig.S6. Typical images showing diffraction-limited fluorescent spots of FLS2-GFP on a fixed cell membrane of *Arabidopsis* leaf epidermal cells under flg22 treatment and co-treatment with MβCD and flg22, imaged with TIRFM.

Fig. S7. Clathrin is required for FLS2 dynamics.

Fig. S8. Clathrin is involved in flg22 induced FLS2 endocytosis.

Fig. S9. FLS2-GFP internalization is perturbed by MβCD.

Fig. S10. Sterols are involved in flg22 induced FLS2 endocytosis.

Fig. S11. Sterols are involved in flg22-induced FLS2 degradation.

Movie S1. VA-TIRFM imaging of FLS2-GFP spots at the plasma membrane of *Arabidopsis* leaf epidermal cells.

Movie S2. VA-TIRFM imaging of FLS2-GFP spots at the plasma membrane of *Arabidopsis* leaf epidermal cells after flg22 treatment.

Movie S3. VA-TIRFM imaging of FLS2-GFP spots in the FLS2-GFP transgenic seedlings in the *smt1* background.

Movie S4. VA-TIRFM imaging of FLS2-GFP spots in *Arabidopsis* leaf epidermal cells treated with 10 mM MβCD.

References

Ali G.S., Prasad K.V., Day I., and Reddy A.S. (2007) Ligand-dependent reduction in the membrane mobility of FLAGELLIN SENSITIVE2, an arabidopsis receptor-like kinase. *Plant Cell Physiol* **48**:1601-1611.

Asai T., Tena G., Plotnikova J., Willmann M.R., Chiu W., LourdesGomez-Gomez L., Boller T., Ausubel F.M., and Sheen J. (2002) MAP kinase signalling cascade in Arabidopsis innate immunity. *Nature* **415**:977-983.

Albrecht C., Boutrot F., Segonzac C., Schwessinger B., Gimenez-Ibanezb S., Chinchillac D., Rathjenb J.P., Vriesa S.C., and Zipfel C. (2012) Brassinosteroids inhibit pathogen-associated molecular pattern-triggered immune signaling independent of the receptor kinase BAK1. *Proc Natl Acad Sci USA* **109**:303-308.

Barbieri E., Fiore P.P.D., and Sigismund S. (2016) Endocytic control of signaling at the plasma membrane. *Curr Opin Cell Biol* **39**:21.

Belkhadir Y., Jaillais Y., Epple P., Balsemão-Piresa E., Dangl J., and Chory J. (2012) Brassinosteroids modulate the efficiency of plant immune responses to microbe-associated molecular patterns. *Proc Natl Acad Sci USA* **109**:297.

Ben K.S., Postma J., and Robatzek S. (2015) A moving view: subcellular trafficking processes in pattern recognition receptor-triggered plant immunity. *Annu Rev Phytopath* **53**:379-402.

Boudsocq M., Willmann M.R., McCormack M., Lee H., Shan L., He P., Bush J., Cheng S., and Sheen J.(2010) Differential innate immune signalling via Ca^{2+} sensor protein kinases. *Nature* **464**:418-422.

Bucherl C.A., Jarsch I.K., Schudoma C., Segonzac C., Mbengue M., Robatzek S., MacLean D., Ott T., and Zipfel C. (2017) Plant immune and growth receptors share common signalling components but localise to distinct plasma membrane nanodomains. *ELife* **6**:1-28

Cacas J.L., Furt F., Guédard M.L., Jean-Marie Schmitte J.M., Buré C., Gerbeau-Pissot P., Patrick Moreau P., Bessoule J.J., Françoise Simon-Plas F., and Mongrand S. (2012) Lipids of plant membrane rafts. *Prog Lipid Res* **51**:272-299.

Carland F., Fujioka S., and Nelson T. (2010) The Sterol Methyltransferases SMT1, SMT2, and SMT3 Influence Arabidopsis Development through Nonbrassinosteroid Products. *Plant Physiol* **153**:741.

Chadda R., Howes M.T., Plowman S.J., Hancock J.F., Parton R.G., and Mayor S. (2007) Cholesterol-sensitive Cdc42 activation regulates actin polymerization for endocytosis via the GEEC pathway. *Traffic* **8**:702-717.

Clayton A.H., Walker F., Orchard S.G., Henderson C., Fuchs D., Rothacker J., Nice E.C., and Burgess A.W. (2005) Ligand-induced dimer-tetramer transition during the activation of the cell surface epidermal growth factor receptor-A multidimensional microscopy analysis. *J Biol Chem* **280**:30392-30399.

Clouse S.D. (2002) *Arabidopsis* mutants reveal multiple roles for sterols in plant development. *Plant Cell* **14**:1995.

Corriden R., Kilpatrick L.E., Kellam B., Briddon S.J., and Hill S.J. (2014) Kinetic analysis of antagonist-occupied adenosine-A3 receptors within membrane microdomains of individual

cells provides evidence of receptor dimerization and allosterism. *FASEB J* **28**:4211-4222.

Danna C.H., and Ausubel F.M. (2011) The Arabidopsis flagellin receptor FLS2 mediates the perception of Xanthomonas Ax21 secreted peptides. *Proc Natl Acad Sci USA* **108**:9286-9291.

Das S.K., Darshi M., Cheley S., Wallace M.I., and Bayley H. (2007) Membrane protein stoichiometry determined from the step-wise photobleaching of dye-labelled subunits. *Chembiochem* **8**:994-999.

Diener A.C., Li H., Zhou W., Whoriskey W.J., Nes W.D., and Fink G.R. (2000) Sterol methyltransferase 1 controls the level of cholesterol in plants. *Plant Cell* **12**:853-870.

DoddsP.N., and Rathjen J.P. (2010) Plant immunity: towards an integrated view of plant-pathogen interactions. *Nat Rev Genet* **11**:539-548.

Doherty G.J., and McMahon H.T. (2009) Mechanisms of endocytosis. *Annu Rev Biochem* **78**:857-902.

Fan L., Li R., Pan J., Ding Z., and Lin J. (2015) Endocytosis and its regulation in plants. *Trends Plant Sci* **20**:388-397.

Felix G., Duran J., Volko S., and Boller T. (1999) Plants have a sensitive perception system for the most conserved domain of bacterial flagellin. *Plant J* **18**:265-276.

Ferrer A., Altabella T., Arró M., and Boronat A. (2017) Emerging roles for conjugated sterols in plants. *Prog Lipid Res* **67**:27-37.

Flores-Otero J., Ahn K.H., Delgado-Peraza F., Mackie K., Kendall D.A., and Yudowski G.A. (2014) Ligand-specific endocytic dwell times control functional selectivity of the cannabinoid receptor 1. *Nat Commu* **5**:4589

Gao J., Wang Y., Cai M., Pan Y., Xu H., Jiang J., Ji H., and Wang H. (2015) Mechanistic insights into EGFR membrane clustering revealed by super-resolution imaging. *Nanoscale* **7**:2511-2519.

Gomez-Gomez L., and Boller T. (2000) FLS2: an LRR receptor-like kinase involved in the perception of the bacterial elicitor flagellin in Arabidopsis. *Mol Cell* **5**:1003-1011.

Grebe M., Xu J., Mobius W., Ueda T., Nakano A., Geuze H.J., Rook M.B., and Scheres B. (2003) Arabidopsis sterol endocytosis involves actin-mediated trafficking via ARA6-positive early endosomes. *Curr Biol* **13**:1378–1387.

Grossie D.A., Turnbull K., Felix-Balderrama S., and Raghavapuram S. (2009) 3-(2-Acetamido-phen-yl)sydnone. *Acta Crystallogr C* **65**:554-555.

Hao H., Fan L., Chen T., Li R., Li X., He Q., Botella M.A., and Lin J. (2014) Clathrin and membrane microdomains cooperatively regulate RbohD dynamics and activity in Arabidopsis. *Plant Cell* **26**:1729-1745

Heese A., Hann D.R., Gimenez-Ibanez S., Jones A., He K., Li J., Schroeder J., Peck S.C., John P., and Rathjen J.P. (2007) The receptor-like kinase SERK3/BAK1 is a central regulator of innate immunity in plants. *Proc Natl Acad Sci USA* **104**:12217-12222.

Henry E., Yadeta K.A., and Coaker G. (2013) Recognition of bacterial plant pathogens: local, systemic and transgenerational immunity. *New Phytol* **199**:908-915.

Heus C.D., Kagie N., Heukers R., Henegouwen P.M., and Gerritsen H.C. (2013) Analysis of EGF receptor oligomerization by homo-FRET. *Method Cell Biol* **117**:305-321.

Hofman E.G., Bader A.N., Voortman J., Heuvel D.J., Sigismund S., Verkleij A.J., Gerritsen H.C., and Henegouwen P.M. (2010) Ligand-induced EGF receptor

oligomerization is kinase-dependent and enhances internalization. *J Biol Chem* **285**:39481-39489.

Irani N.G., and Russinova E. (2009) Receptor endocytosis and signaling in plants. *Curr Opin Plant Biol* **12**:653-659.

Keinath N.F., Kierszniowska S., Lorek J., Bourdais G., Sharon A. Kessler S.A.,Hiroko Shimosato-Asano H., Grossniklaus U., Schulze W.X., Robatzek S., and Panstruga R. (2010) PAMP (pathogen-associated molecular pattern)-induced changes in plasma membrane compartmentalization reveal novel components of plant immunity. *J Biol Chem* **285**: 39140-39149.

Kopischke M., Westphal L., Schneeberger K., Clark R., Stephan O.S., Wewer V., Fuchs R., Landtag J., Hause G., Dörmann P., et al, (2013) Impaired sterol ester synthesis alters the response of Arabidopsis thaliana to Phytophthora infestans. *Plant J* **73**:456-468.

Kunze G., Zipfel C., Robatzek S., Niehaus K., Boller T., and Felix G. (2004) The N terminus of bacterial elongation factor Tu elicits innate immunity in Arabidopsis plants. *Plant Cell* **16**:3496-3507.

Li L., Li M., Yu L., Yu L.Y., Zhou Z.Y., Liang X.X., Liu Z.X., Cai G.H., Gao L.Y., Zhang X.J, Wang Y.C, et al. (2014) The FLS2-associated kinase BIK1 directly phosphorylates the NADPH oxidase RbohD to control plant immunity. *Cell Host Microbe* **15**:329-338.

Li R., Liu P., Wan Y., Chen T., Wang Q., Mettbach U., Baluška F., Samaj J., Fang X., Lucas W.J., and Lin J. (2012) A membrane microdomain-associated protein, Arabidopsis Flot1, is involved in a clathrin-independent endocytic pathway and is required for seedling development. *Plant Cell* **24**:2105-2122.

Li X., Wang X., Yang Y., Li R., He Q., Fang X., Luu D., Maurel C., and Lin J. (2011) Single-molecule analysis of PIP2;1 dynamics and partitioning reveals multiple modes of Arabidopsis plasma membrane aquaporin regulation. *Plant Cell* **23**:3780-3797.

Low-Nam S.T., Lidke K.A., Cutler P.J., Roovers R.C., Henegouwen P., Wilson B.S., and Lidke D.S. (2011) ErbB1 dimerization is promoted by domain co-confinement and stabilized by ligand binding. *Nat Struct Mol Biol* **18**:1244-1249.

Malinsky J., Opekarova M., Grossmann G., and Tanner W.(2013) Membrane microdomains, rafts, and detergent-resistant membranes in plants and fungi. *Annu Rev Plant Biol* **64**:501-529.

Mbengue M., Bourdais G., Gervasi F., Beck M., Zhou J., Spallek T., Bartels S., Boller T., Ueda T., Kuhna H., and Robatzek S. (2016) Clathrin-dependent endocytosis is required for immunity mediated by pattern recognition receptor kinases. *Proc Natl Acad Sci USA* **113**:11034-11039.

Men S., Boutté Y., Ikeda Y., Li X., Palme K., Stierhof Y.D., Hartmann M.A., Moritz T., and Grebe M. (2008) Sterol-dependent endocytosis mediates post-cytokinetic acquisition of PIN2 auxin efflux carrier polarity. *Nat Cell Biol* **10**:237-244.

Monaghan J.,and Zipfel C. (2012) Plant pattern recognition receptor complexes at the plasma membrane. *Curr Opin Plant Biol* **15**:349-357.

Mulder L., Lefebvre B., Cullimore J., and Imberty A. (2006) LysM domains of Medicago truncatula NFP protein involved in Nod factor perception. Glycosylation state, molecular modeling and docking of chitooligosaccharides and Nod factors. *Glycobiology* **16**:801-809.

Naramoto S., Kleine-Vehn J., Robert S., Fujimoto M., Dainobu T., Paciorek T., Ueda T.,

Nakano A., Van Montagu M.C., Fukuda H., and Friml J. (2010) ADP-ribosylation factor machinery mediates endocytosis in plant cells. *Proc Natl Acad Sci USA* **107**:21890–21895.

Ortiz-Morea F.A., Savatin D.V., Dejonghe W., Kumar R., Luo Y., Adamowski M., Van den Begin J., Dressano K., Pereira de Oliveira G., et al..(2016) Danger-associated peptide signaling in Arabidopsis requires clathrin. *Proc Natl Acad Sci USA* **113**:11028-11033.

Radutoiu S., Madsen L.H., Madsen E.B., Jurkiewicz A., Fukai E., Quistgaard E.M., Albrektsen A.S., James E.K., Thirup S., and Stougaard J. (2007) LysM domains mediate lipochitin-oligosaccharide recognition and Nfr genes extend the symbiotic host range. *EMBO J* **26**:3923-3935.

Robatzek S., Chinchilla D.,and Boller T. (2006) Ligand-induced endocytosis of the pattern recognition receptor FLS2 in Arabidopsis. *Gene Dev* **20**:537-542.

Roux M., Schwessinger B., Albrecht C., Chinchilla D., Jones A., Holton N., Malinovsky F.G., Tör M., Vries S., and Zipfel C.(2011) The Arabidopsis leucine-rich repeat receptor-like kinases BAK1/SERK3 and BKK1/SERK4 are required for innate immunity to hemibiotrophic and biotrophic pathogens. *Plant Cell* **23**:2440-2455.

Saka S.K., Honigmann A., Eggeling C., Hell S.W., Lang T., and Rizzoli S.O. (2014) Multi-protein assemblies underlie the mesoscale organization of the plasma membrane. *Nat Commun* **5**:4509.

Schlessinger J.(2002) Ligand-induced, receptor-mediated dimerization and activation of EGF receptor. *Cell* **110**:669-672.

Segonzac C., and Zipfel C. (2011) Activation of plant pattern-recognition receptors by bacteria. *Curr Opin Microbio***l14**:54-61.

Sigismund S., Argenzio E., Tosoni D., Cavallaro E., Polo S., and Di Fiore P.P. (2008) Clathrin-mediated internalization is essential for sustained EGFR signaling but dispensable for degradation. *Dev Cell* **15**:209-219.

Simons K., and Toomre D.(2000) Lipid rafts and signal transduction. *Nat Rev Mol Cell Bio* **1**:31-39.

Stanislas T., Bouyssie D., Rossignol M., Vesa S., Fromentin J., Morel J., Pichereaux C., Monsarrat B., and Simon-Plas F. (2009) Quantitative proteomics reveals a dynamic association of proteins to detergent-resistant membranes upon elicitor signaling in Tobacco. *Mol Cell Proteomics* **8**:2186.

Stanislas T, Grebe M, Boutté Y. (2014) Sterol Dynamics During Endocytic Trafficking in Arabidopsis. *Methods Mol Biol* **1209**:13-29.

Sun Y., Li L., Macho A.P., Han Z., Hu Z., Zipfel C., Zhou J.M., and Chai J. (2013) Structural basis for flg22-induced activation of the *Arabidopsis* FLS2-BAK1 immune complex. *Science* **342**:624-628.

Ulbrich M.H., and Isacoff E.Y. (2007) Subunit counting in membrane-bound proteins. *Nat Methods* **4**:319-321.

Wang C., Yan X., Chen Q., Jiang N., Fu W., Ma B., Liu J., Li C., Bednarek S.Y., and Pan J. (2013) Clathrin Light Chains Regulate Clathrin-Mediated Trafficking, Auxin Signaling, and Development in Arabidopsis. *Plant Cell* **25**:499-516.

Wang L., Li H., Lv X., Chen T., Li R., Xue Y., Jiang J., Jin B., Baluš ka F., Samaj J., Wang X., and Lin J. (2015) Spatiotemporal dynamics of the BRI1 receptor and its regulation by membrane microdomains in living Arabidopsis cells. *Mol Plant* **8**:1334-1349.

Wang L., Xue Y., Xing J., Song K., and Lin J. (2018) Exploring the spatiotemporal organization of membrane proteins in living plant cells. *Annu Rev Plant Biol* **69**:525-551

Willemsen V., Friml J., Grebe M., Toorn A., Palme K., and Scheres B. (2003) Cell polarity and PIN protein positioning in Arabidopsis require STEROL METHYLTRANSFERASE1 function. *Plant Cell* **15**: 612–625

Xue Y., Xing J., Wan Y., Lv X., Fan L., Zhang Y., Song K., Wang L., Wang X., Deng X. et al. (2018) Arabidopsis blue light receptor phototropin 1 undergoes blue light-induced activation in membrane microdomains. *Mol Plant* **11**:846–859.

Yadeta K.A., Elmore J.M., and Coaker G. (2013) Advancements in the analysis of the Arabidopsis plasma membrane proteome. *Front Plant Sci* **4**:86.

Yeh Y.H., Chang Y.H., Huang P.Y., Huang J.B., and Zimmerli L. (2015) Enhanced Arabidopsis pattern-triggered immunity by overexpression of cysteine-rich receptor-like kinases. *Front Plant Sci* **6**:322

Yu M., Liu H., Dong Z., Xiao J., Su B., Fan L., Komis G., Šamaj J., Lin J., and Li R. (2017) The dynamics and endocytosis of Flot1 protein in response to flg22 in Arabidopsis. *J Plant Physiol* **215**:73.

Zinchuk V., Wu Y., Grossenbacher-Zinchuk O., and Stefani E. (2011) Quantifying spatial correlations of fluorescent markers using enhanced background reduction with protein proximity index and correlation coefficient estimations. *Nat Protoc* **6**:1554-1567.

Figures

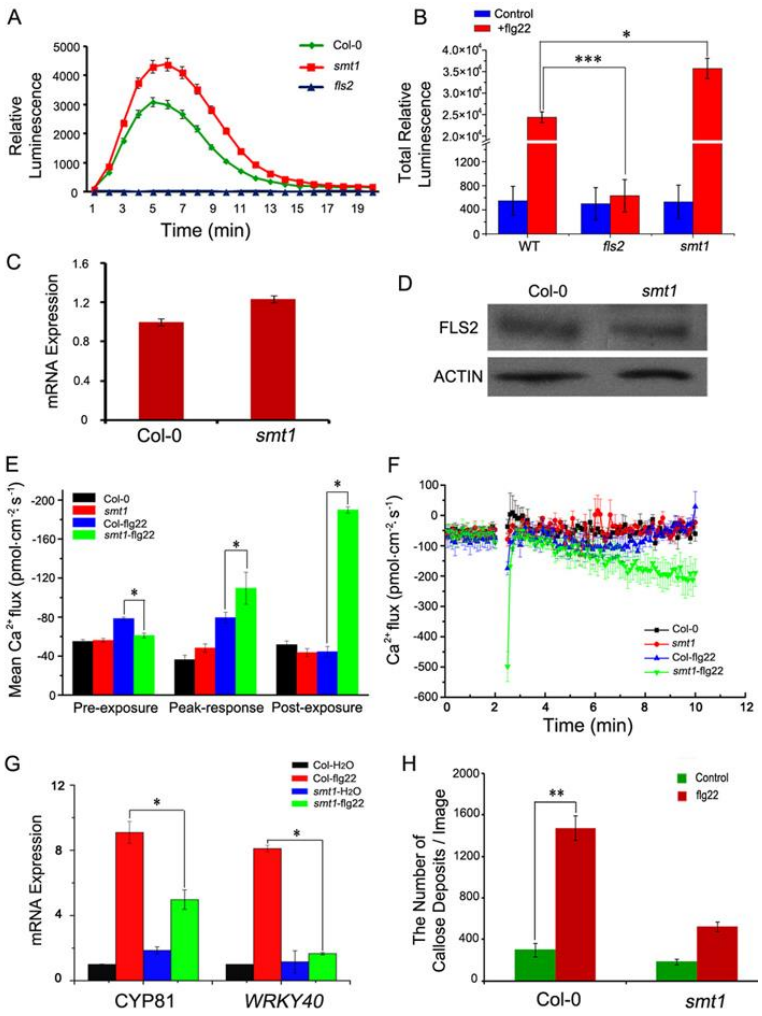

Fig. 1. Flg22-induced defense response is impaired in the sterol-deficient *smt1* mutant.

(A) Reactive oxygen species (ROS) burst in response to flg22 measured as relative luminescence from a luminol-based assay at different times after flg22 treatment. Experiments were repeated independently at least twice, with similar results.

(B) Total ROS production (as RLU) in Col-0, *fls2*, and *smt1* are shown before and after flg22 treatment in 16 rosette leaf disks. The experiment was

performed twice with consistent results. For the ROS burst (A and B), relative amounts of H_2O_2 (expressed as relative luminescence) were measured immediately. Experiments were repeated independently at least twice, with similar results. Error bars represent the SD. Values are means ± SDs (n = 8). Statistical significance was checked by Student's *t*-test (*P < 0.05 and ***P < 0.001).

(C) The expression of *FLS2* by quantitative real-Time PCR (qRT-PCR) with *ACTIN* as the reference gene, mRNA levels of *FLS2* were not significantly different between *smt1* and Col-0. Experiments were repeated independently at least twice, with similar results. Error bars represent the SD.

(D) Protein levels of FLS2 measured by immunoblot analysis of *Arabidopsis* plant.

(E) The mean Ca^{2+} fluxes of Col-0 and *smt1* before exposure to flg22, in response to flg22 and after exposure to flg22. Error bars represent the SD. Statistical significance was checked by Student's *t*-test (*P <0.05).

(F) The flg22-induced Ca^{2+} flux in Col-0 and *smt1*. A continuous Ca^{2+} flux recording of 10 min was conducted for each cell in test media. Each point represents the mean for 8-10 individual plants and bars represent the standard error of the mean. Error bars represent the SD.

(G) mRNA levels of *CYP81* and *WRKY40* were significantly different between Col-0 and *smt1* at 30 minutes after elicitation with mock or 10 µM flg22. For qRT-PCR, ten-day-old *Arabidopsis* Col-0 were treated with flg22 for the indicated time. Experiments were repeated independently at least twice, with similar results. Error bars represent the SD. Statistical significance was checked by Student's *t*-test (*P <0.05).

(H) Quantification of aniline blue-stained callose deposits in Col-0 and *smt1* without and with 2 µM flg22 treatment (Untreated, n = 9 images; flg22 treated, n = 12 images). Error bars represent the SD. Statistical significance was checked by Student's *t*-test (*P < 0.05).

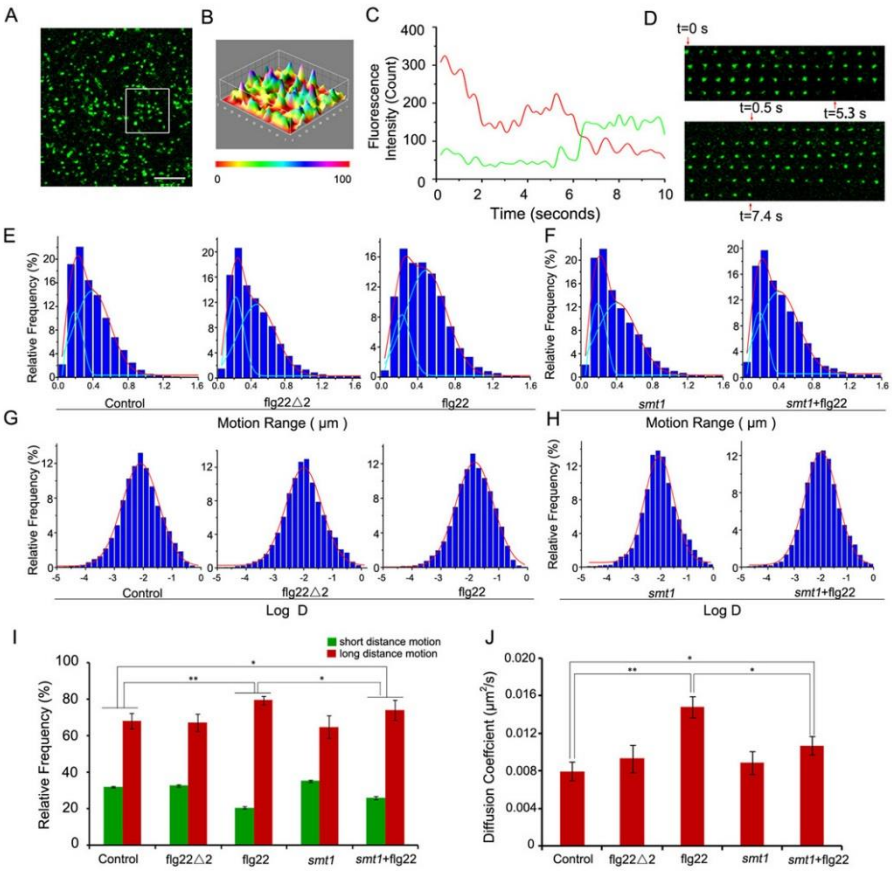

Fig. 2 Effects of sterols on the dynamics of FLS2-GFP spots at the plasma membrane.

(A) A typical single-particle image of FLS2-GFP at the plasma membrane of living cells. Scale bar = 5 μm.

(B) Three-dimensional luminance plots of the FLS2-GFP spots in (A) showing varied fluorescence intensity among different spots.

(C) Fluorescence intensity tracks of single FLS2-GFP particles showing their disappearance and appearance.

(D) FLS2-GFP spots appeared at different time, stayed for a short or longer time then disappearance.

(E) Distribution of FLS2-GFP motion range under control (n = 7382 spots), flg22Δ2 (a flg22-derived peptide lacking the agonist activity of flg22) (15 min) (n = 9753 spots), flg22 (15 min) (n = 11072 spots) treatment.

(F) Distribution of FLS2-GFP motion range in *smt1* mutant seedlings (n = 8970 spots) and in *smt1* mutant seedlings after flg22 (15 min) (n = 12331 spots) treatment.

(G) Distribution of FLS2-GFP diffusion coefficients under control (n = 7787 spots), flg22Δ2 (15 min) (n = 12694 spots), flg22 (15 min) (n = 11073 spots) treatment.

(H) Distribution of FLS2-GFP diffusion coefficients in *smt1* mutant seedlings (n = 6511 spots) and in *smt1* mutant seedlings after flg22 (15 min) (n = 13357 spots) treatment.

(I) Frequency of long distance and short distance motions for FLS2-GFP under different environment. Error bars represent the SD. Statistical significance was checked by Student's *t*-test (*P < 0.05 and **P < 0.01).

(J) Diffusion coefficients of FLS2-GFP under different environment. Error bars represent the SD. Statistical significance was checked by Student's *t*-test (*P < 0.05 and **P < 0.01).

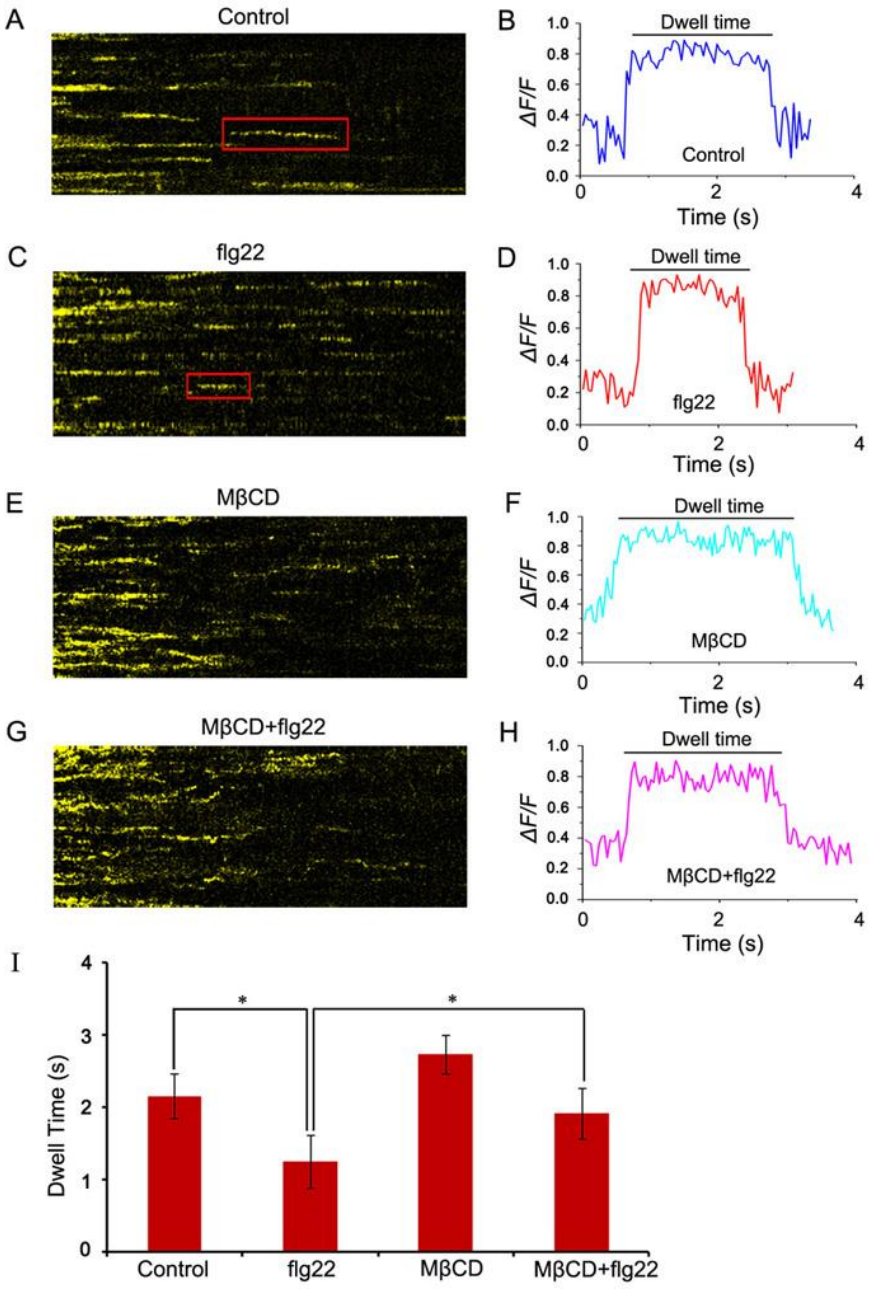

Fig. 3. Different environment induce specific dwell times of the FLS2.

(A, C, E, G) Representative kymograph showing individual FLS2-GFP dwell times in the presence of the control (A), flg22 (C), MβCD (E), MβCD and flg22 co-treatment (G).

(B, D, F, H) Representative traces of normalized fluorescence from the control (B), flg22 (D), MβCD (F), MβCD and flg22 co-treatment (H).

(I) Dwell times were analyzed under the control, flg22, MβCD, MβCD and flg22 co-treatment. Error bars represent the SD. Statistical significance was checked by Student's *t*-test (*P < 0.05).

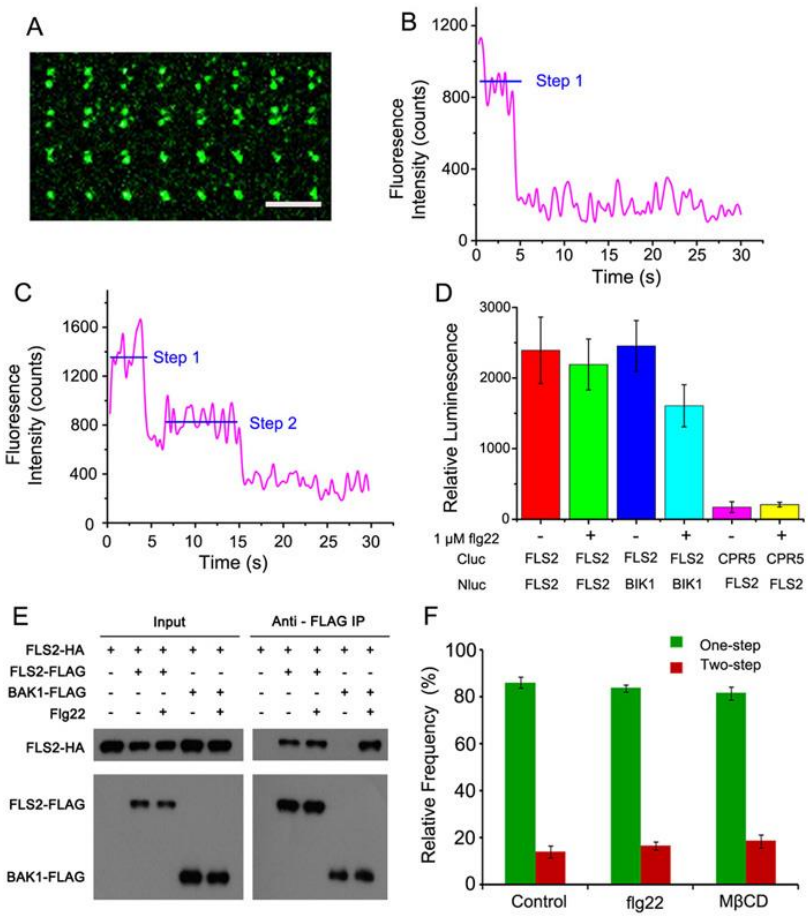

Fig. 4 FLS2 aggregation status.

(A) Series of images from single-particle live-cell imaging showing two FLS2-GFP spots merging. Bar = 5 μm.

(B) Time course of GFP emission after background correction showing one-step bleaching.

(C) Time course of GFP emission after background correction showing two-step bleaching.

(D) FLS2 aggregation status using split-luciferase assays in *N. benthamiana*. Split-luciferase assays were conducted in the presence or absence of flg22. Co-expression of Cluc-CPR5 and FLS2-Nluc was used as a negative control while co-expression of FLS2-Cluc and BIK1-Nluc served as a positive control. Experiments were repeated independently at least twice, with similar results. The '+' indicates applied flg22 treatment and the '-' represents no peptide

treatment. Values represent mean relative luminescence units (RLU) ± SDs (n = 8).

(E) The interaction between FLS2 and FLS2 confirmed by co-immunoprecipitation assays in *Arabidopsis* protoplasts. The FLS2-HA construct was co-expressed with FLS2-FLAG or BAK1-FLAG in *Arabidopsis* protoplasts. FLS2-HA was present in the FLS2-FLAG immune complex before and after flg22 treatment. Furthermore, using FLS2-HA plus BAK1-FLAG as a positive control, the FLS2-HA only appeared in flg22-induced BAK1-FLAG complex. In contrast, using FLS2-HA as a negative control, FLS2-HA did not appear in FLAG complex both before and after flg22 treatment. The '+' indicates applied flg22 treatment, in contrast, the '-' represents no peptide treatment. The experiment was repeated three times, and data of one representative experiment are shown.

(F) Ratio of FLS2 monomer and dimer before (n = 428 spots) and after (n = 435 spots) flg22 treatment. Error bars represent the SD.

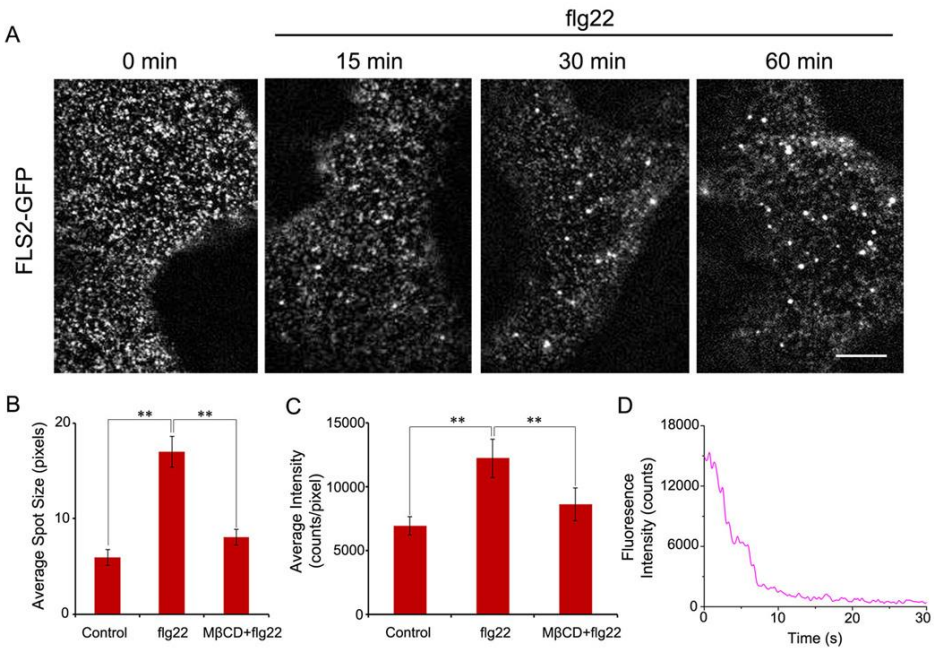

Fig. 5 Flg22-induced FLS2-GFP forms receptor clusters in a time-dependent manner at the plasma membrane.

(A) Typical images showing diffraction-limited fluorescent spots of FLS2-GFP on fixed cell membrane of *Arabidopsis* leaf epidermis cells with flg22 treatment for 15, 30, and 60 min, imaged with TIRFM. The image is a section of the first frame of a stack of images with the background subtracted. (Scale bar = 1 μm) (B–C) Average size (B) and fluorescence intensity (C) of FLS2-GFP fluorescent spots under control (n = 178), flg22 treatment (n = 239), MβCD and flg22 co-treatment (n = 247), showing that flg22 induced the massing of FLS2-GFP oligomers into clusters. Error bars represent the SD. Statistical significance was checked by Student's *t*-test (*P < 0.05).

(D) Representative time course of FLS2-GFP spots under flg22 treatment in *Arabidopsis* leaf cells, showing the approximately exponential distribution of the bleaching steps.

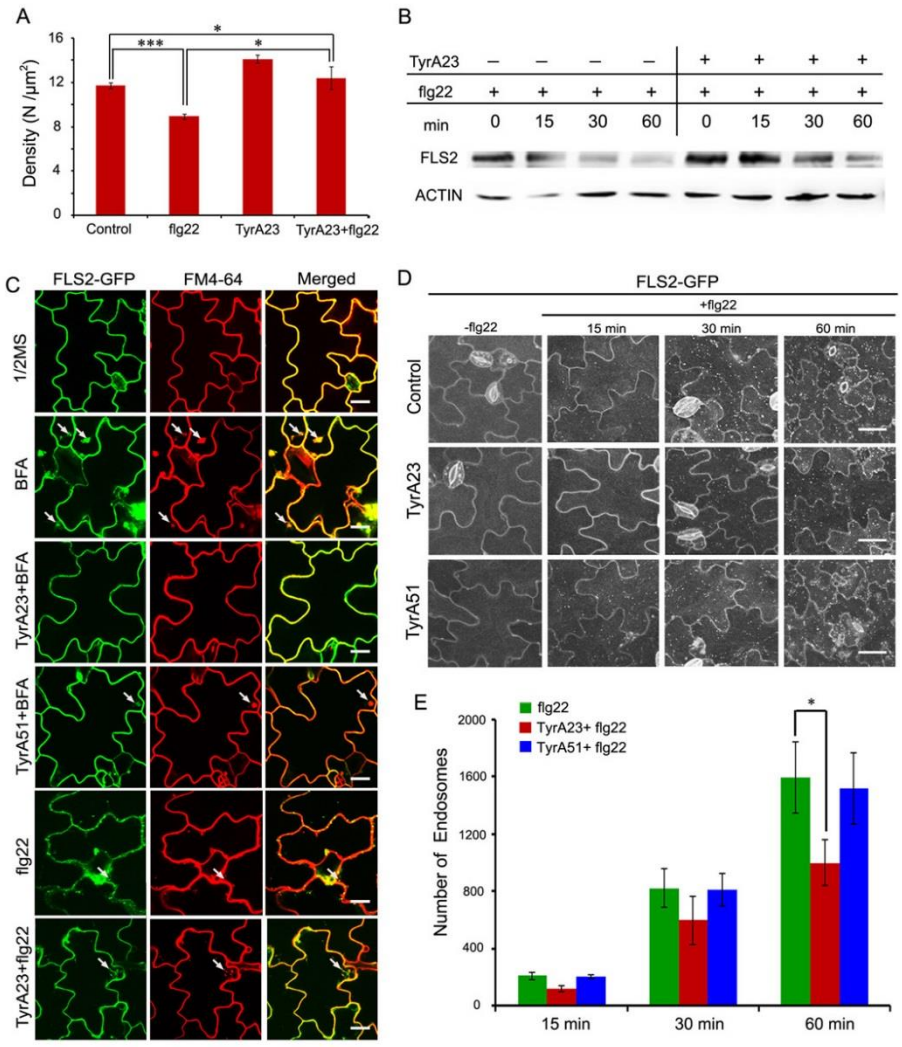

Fig. 6 TyrA23 affects the internalization of FLS2-GFP.

(A) The density of FLS2-GFP particles in the different treatment was measured by FCS (n = 30 cells from five seedlings for each treatment). Error bars represent the SD. Statistical significance was checked by Student's *t*-test (*P < 0.05 and ***P < 0.001).

(B) Immunoblot analysis of FLS2 protein levels under flg22, flg22 and TyrA23 co-treatment for 15, 30, 60 min.

(C) FLS2-GFP subcellular localization in the presence of the indicated chemical inhibitors and ligands. The left photographs represent GFP signal showing subcellular localization of FLS2-GFP in the presence of the indicated chemicals and ligands. The middle photographs represent red fluorescence signal showing the plasma membrane stained by FM4-64. The right

photographs represent the merge of FLS2-GFP and FM4-64 staining. Arrows indicate BFA bodies and FLS2 endosomes (n = 15 cells from five seedlings foreach treatment). Bar = 10 µm.

(D) Confocal image of *Arabidopsis* leaf epidermis with FLS2-GFP treated with flg22, TyrA23 and flg22, TyrA51 and flg22, co-treatment for 15, 30, 60 min; Bar = 20 µm.

(E) Quantitative analysis of FLS2-GFP endosomal spots per image in response to flg22 treatment over time. (n = three seedlings for each treatment). Error bars represent the SD. Statistical significance was checked by Student's *t*-test (*P < 0.05).

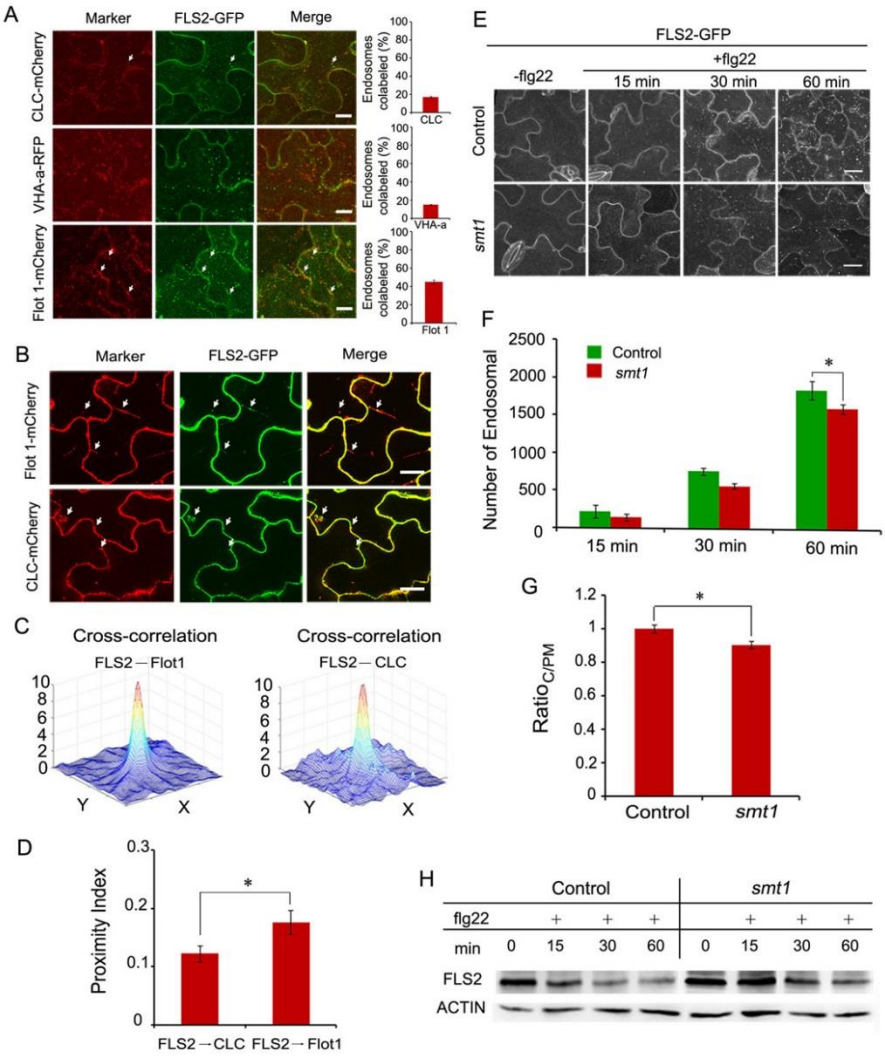

Fig. 7 Endocytosis of FLS2 is associated with sterols.

(A) Colocalization of FLS2-GFP vesicles with the CLC-mCherry, VHA-a1-RFP, Flot 1-mCherry in crossed transgenic lines (n = three seedlings for each treatment). Bar = 20 μm.

(B) FLS2-GFP colocalized with Flot1/CLC-mCherry in crossed transgenic lines. Arrows indicate endosomes showing colocalization (n = three seedlings for each treatment). Bar = 20 μm

(C) 3D plot of FLS2-GFP and Flot1/CLC-mCherry cross-correlation versus pixel shift.

(D) Mean protein proximity indexes showing FLS2-Flot1/CLC degree of proximity under flg22 treatment (n=39). Experiments were repeated independently at least twice, with similar results. Error bars represent the SD.

Statistical significance was checked by Student's *t*-test (*P < 0.05).

(E) In *smt1* mutants, confocal image of *Arabidopsis* leaf epidermis with FLS2-GFP treated with flg22 for 15, 30, 60 min. Bar = 20 μm.

(F) In *smt1* mutants, quantitative analysis of FLS2-GFP endosomal spots per image in response to flg22 treatment over time. (n = three seedlings for each treatment). Error bars represent the SD. Statistical significance was checked by Student's *t*-test (*P < 0.05).

(G) Quantification of FLS2 endocytosis as estimated by the ratio of the average signal intensity in the cytosol over that at the PM (n=54). Experiments were repeated independently at least thrice, with similar results. Error bars represent the SD. Statistical significance was checked by Student's *t*-test (*P < 0.05).

(H) Immunoblot analysis of FLS2 protein levels under flg22 treatment for 15, 30, 60 min in control and *smt1* mutants.

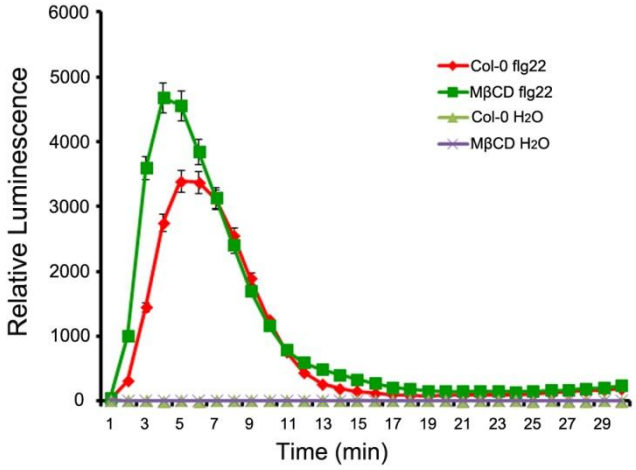

Fig. S1. MβCD affected flg22-induced ROS production.

In time-course experiments, ROS production was elevated under flg22 and MβCD co-treatment compared to flg22 treatment (Values are means ± SDs; n $\geqslant$ 4; three biological repeats).

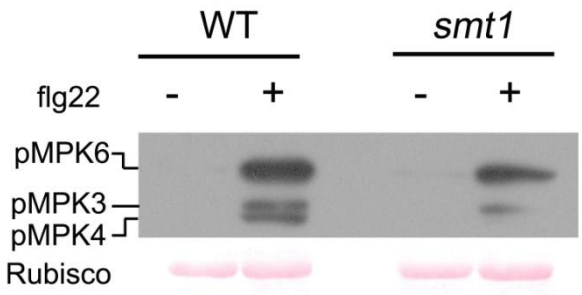

Fig. S2. Detection of the MAPKs phosphorylation in *Arabidopsis thaliana* in response to flg22 in WT and *smt1* mutants. No phosphorylated MAPKs were detected in the untreated sample (-).

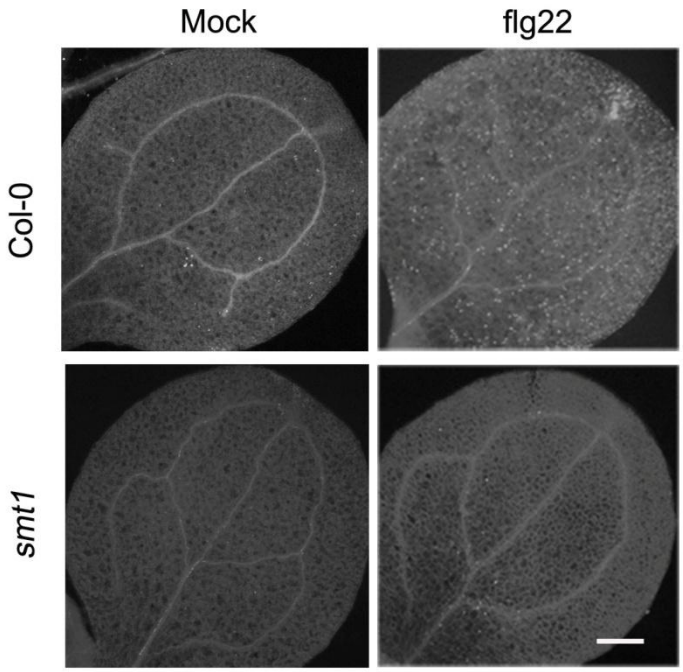

Fig. S3. Flg22 induced callose deposition.

Callose deposition in 2-week-old leaf tissue of the WT and the *smt1* mutants at 24 hr after infiltration with flg22. Representative images are shown depicting differences in callose deposition between Col-0 and *smt1* mutants under mock and flg22 treatments. Scale bar = 0.5 mm (Untreated, n = 9 images; flg22 treated, n = 12 images from two biological replicates).

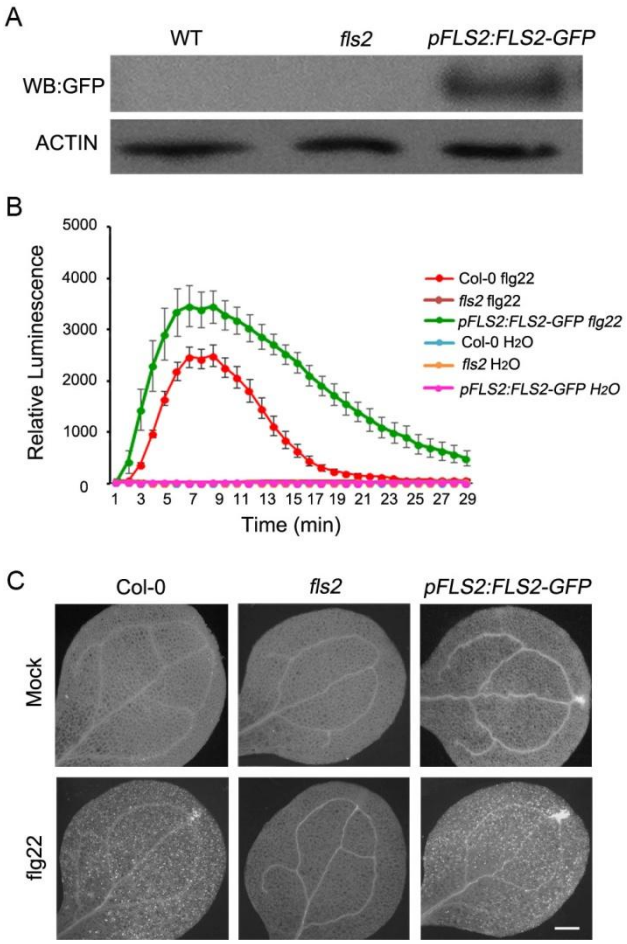

Fig. S4. Rescue of the *fls2* mutant by a genomic sequence of *FLS2* fused with the *GFP* sequence in *Arabidopsis* leaves.

(A) Immunoblot analysis of total protein extracts from WT, *fls2* (as a control) and FLS2-GFP transgenic *Arabidopsis* seedlings probed with GFP and ACTIN antibodies.

(B) Flg22-triggered (100 nM) ROS burst in Col-0, *fls2*, and pFLS2:FLS2-GFP transgenic seedlings. (Values are means ± SDs; n ⩾ 4; two biological repeats)

(C) Measurement of callose deposition in Col-0, *fls2*, and pFLS2:FLS2-GFP transgenic seedlings using aniline blue staining under mock or 2 μM flg22 treatment for 24 h. Bar =200 μm. (Untreated, n = 9 images; flg22 treated, n = 17 images pooled from two biological replicates)

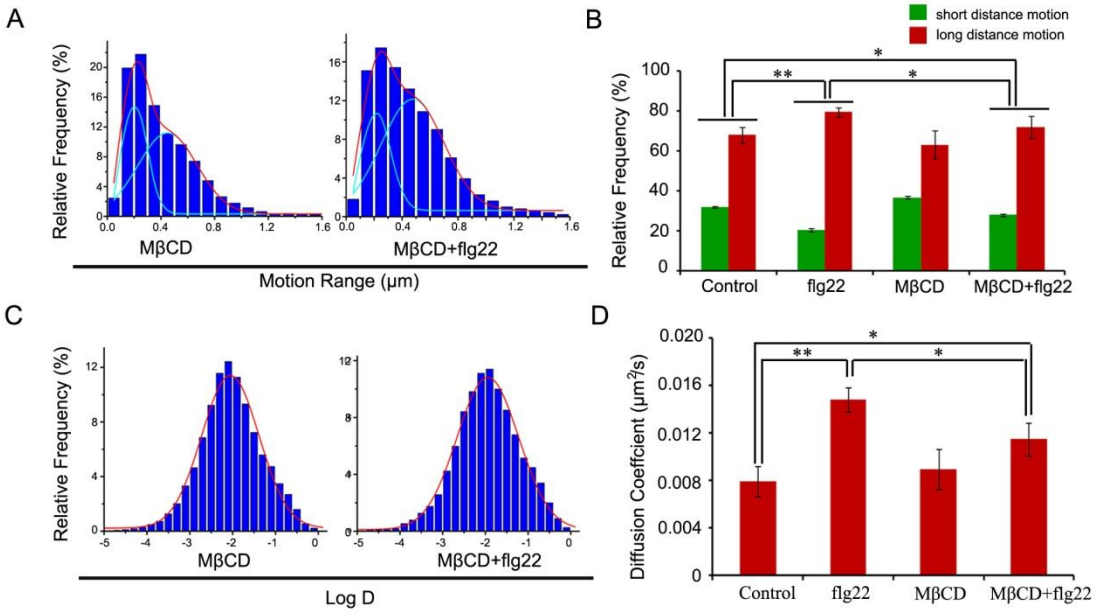

Fig. S5. Effects of MβCD treatment on the dynamic behavior of FLS2-GFP.

(A) Distribution of motion ranges of FLS2-GFP spots under MβCD (n = 10811 spots), MβCD and flg22 co-treatment (n = 7738 spots), respectively.

(B) Frequency of long distance and short distance motions for FLS2-GFP under different treatments. Error bars represent the SD. Statistical significance was checked by Student's *t*-test (*P <0.05).

(C) Distribution of diffusion coefficients of FLS2-GFP spots under MβCD (n = 12592 spots), MβCD and flg22 co-treatment (n = 9610 spots), respectively.

(D) Diffusion coefficients of FLS2-GFP spots under different treatments. Error bars represent the SD. Statistical significance was checked by Student's *t*-test (*P <0.05 and **P < 0.01).

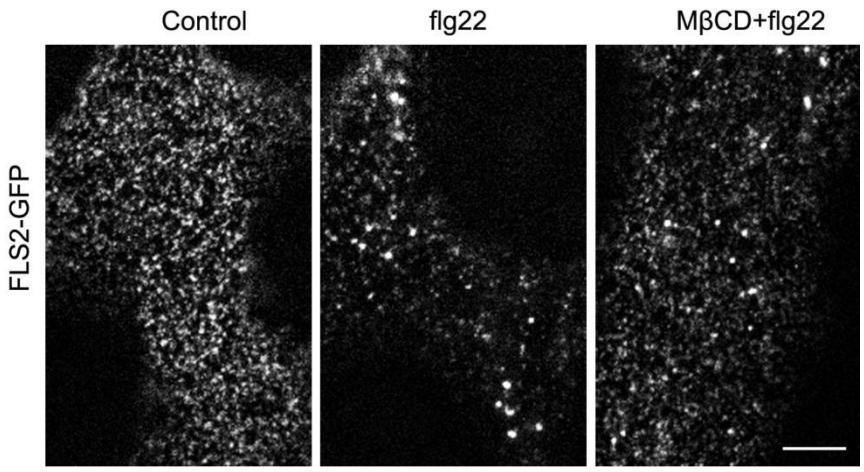

Fig. S6. Typical images showing diffraction-limited fluorescent spots of FLS2-GFP on a fixed cell membrane of *Arabidopsis* leaf epidermal cells under flg22 treatment and co-treatment with MβCD and flg22, imaged with TIRFM. The image is a section of the first frame of a stack of images with the background subtracted (Scale bar: 1 µm).

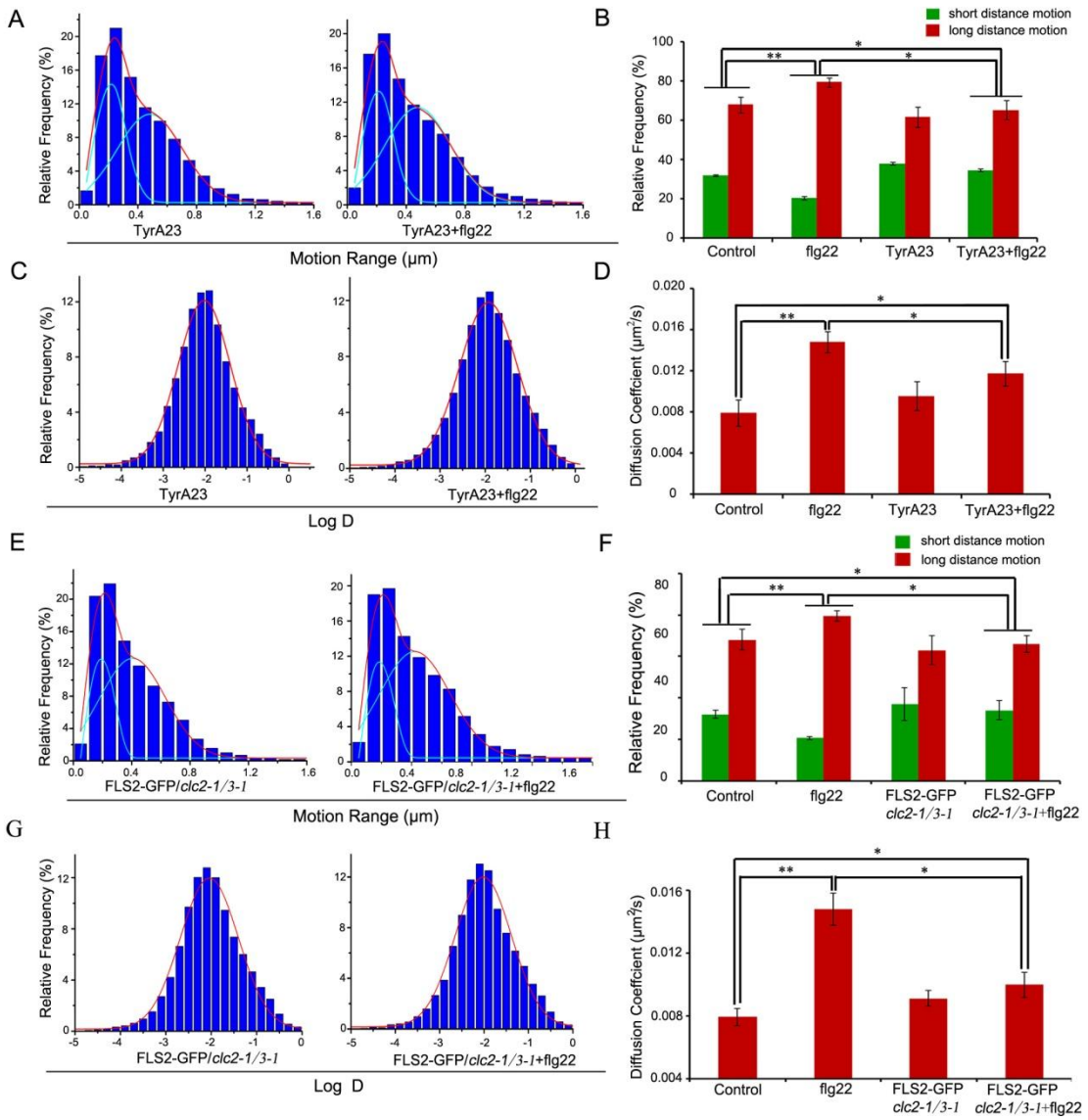

Fig. S7. Clathrin is required for FLS2 dynamics.

(A) Distribution of FLS2-GFP motion range under TyrA23 treatment (n = 14401 spots), TyrA23 and flg22 co-treatment (n = 11445 spots).

(B) Frequency of long distance and short distance motions for FLS2-GFP under different treatments. Error bars represent the SD. Statistical significance was checked by Student's *t*-test (*P <0.05 and **P < 0.01).

(C) Distribution of FLS2-GFP diffusion coefficients under TyrA23 treatment (n = 17147 spots), TyrA23 and flg22 co-treatment (n = 28319 spots).

(D) Diffusion coefficients of FLS2-GFP under different treatments. Error bars represent the SD. Statistical significance was checked by Student's *t*-test (*P <0.05 and **P < 0.01).

(E) Distribution of FLS2-GFP motion range in *clc2-1 clc3-1* mutant (n = 9870 spots) and in *clc2-1 clc3-1* mutant seedlings after flg22 (n = 11342 spots).

(F) Frequency of long distance and short distance motions for FLS2-GFP in *clc2-1 clc3-1* mutant. Error bars represent the SD. Statistical significance was checked by Student's *t*-test (*P <0.05 and **P < 0.01).

(G) Distribution of FLS2-GFP diffusion coefficients in *clc2-1 clc3-1* mutant (n = 9311 spots) and in *clc2-1 clc3-1* mutant seedlings after flg22 (n = 12776 spots).

(H) Diffusion coefficients of FLS2-GFP in *clc2-1 clc3-1* mutant. Error bars represent the SD. Statistical significance was checked by Student's *t*-test (*P <0.05 and **P < 0.01).

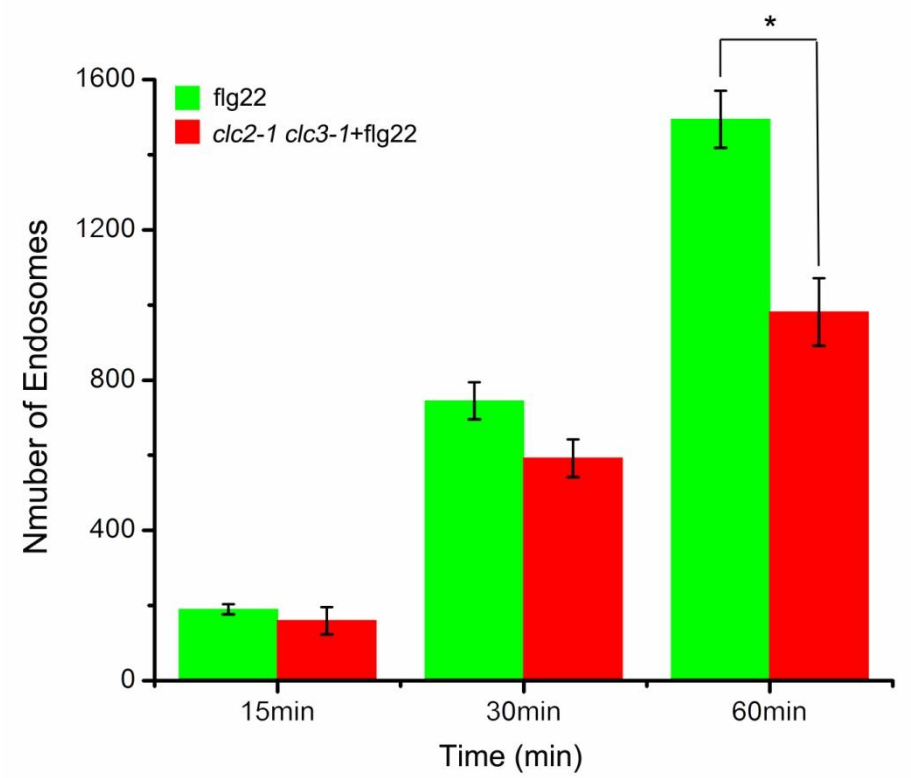

Fig. S8. Clathrin is involved in flg22 induced FLS2 endocytosis.

In *clc2-1 clc3-1* mutant, FLS2-GFP endosome numbers per image area in response to flg22 treatments over time (n = three seedlings for each treatment). Error bars represent the SD. Statistical significance was checked by Student's *t*-test (*P <0.05).

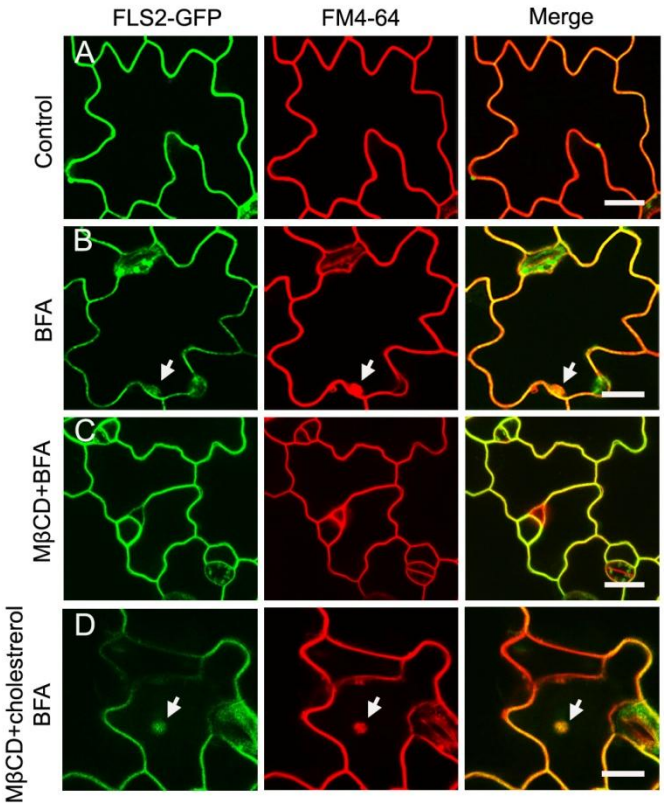

Fig. S9. FLS2-GFP internalization is perturbed by MβCD.

(A) FLS2-GFP co-localized with FM4-64 at the plasma membrane.

(B) FLS2-GFP colocalized with FM4-64 in BFA compartment after BFA treatment.

(C) MβCD reduced the BFA-induced intracellular accumulation of FLS2-GFP.

(D) The effects of sterol complement on FLS2 internalization. Cholesterol was replenished in depleted cells by incubating them with MβCD-cholesterol complexes.

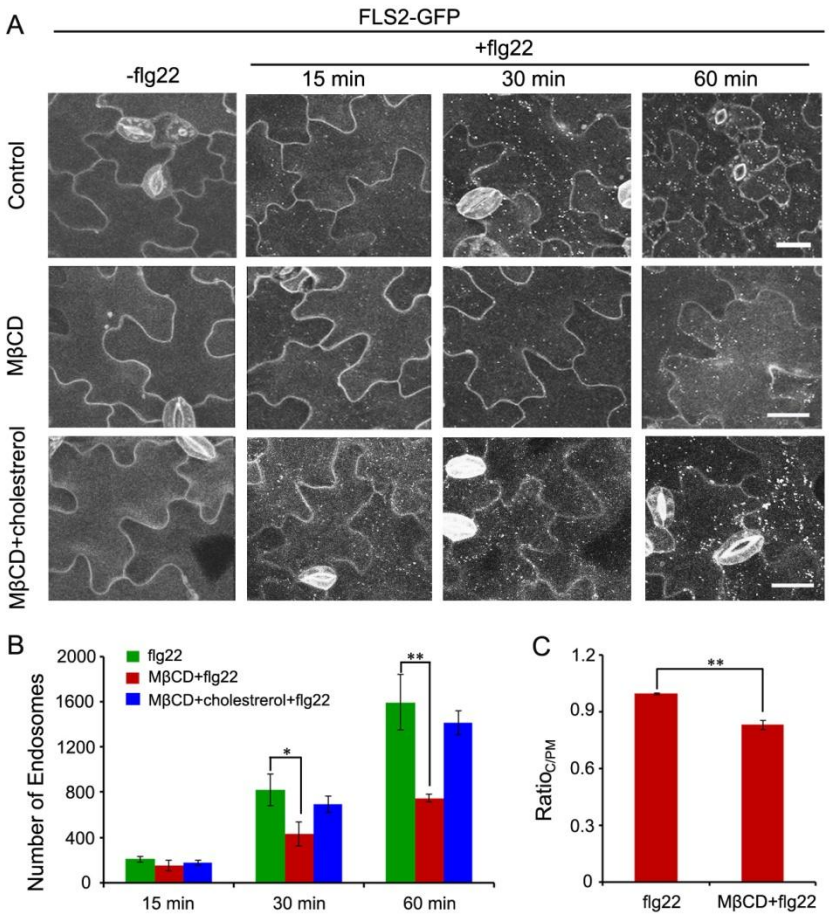

Fig. S10. Sterols are involved in flg22 induced FLS2 endocytosis.

(A) Confocal images of FLS2-GFP treated with flg22, MβCD, MβCD coupled with flg22, or MβCD andMβCD-cholesterol complexes coupled with flg22 co-treatment for 15, 30, and 60 min in *Arabidopsis* leaf epidermis, Bar = 20μm.

(B) FLS2-GFP endosome numbers per image area in response to various treatments over time (n = three seedlings for each treatment). Error bars represent the SD. Statistical significance was checked by Student's *t*-test (*P <0.05 and **P < 0.01).

(C) Quantification of FLS2 endocytosis as estimated by the ratio of the average signal intensity in the cytosol over that at the PM under different conditions (n=33). Error bars represent the SD. Statistical significance was checked by Student's *t*-test (**P < 0.01).

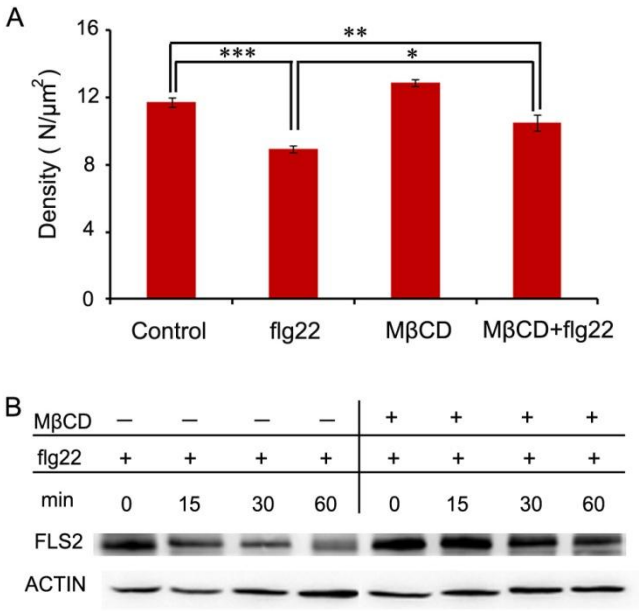

Fig. S11 Sterols are involved in flg22-induced FLS2 degradation.

(A) The density of FLS2-GFP molecules in the different treatments was measured by FCS (n = 30 cells from five seedlings for each treatment). Error bars represent the SD. Statistical significance was checked by Student's *t*-test (*P <0.05, **P < 0.01 and ****P* < 0.001).

(B) Immunoblot analysis of FLS2 protein levels under flg22, flg22 and MβCD co-treatment for 15, 30, and 60 min.

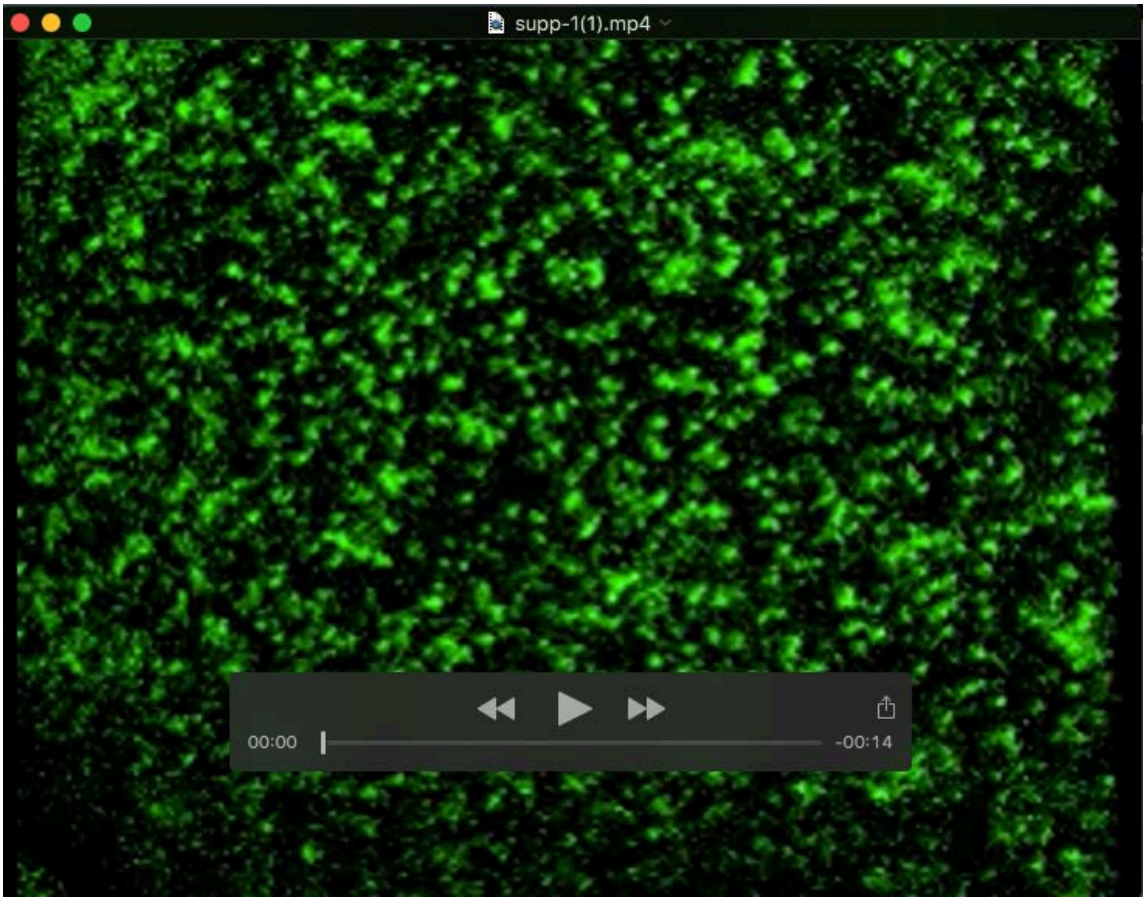

Movie S1. VA-TIRFM imaging of FLS2-GFP spots at the PM of *Arabidopsis* leaves epidermal cells. Movies of 100 frames were acquired; exposure time for each frame was 100 ms.

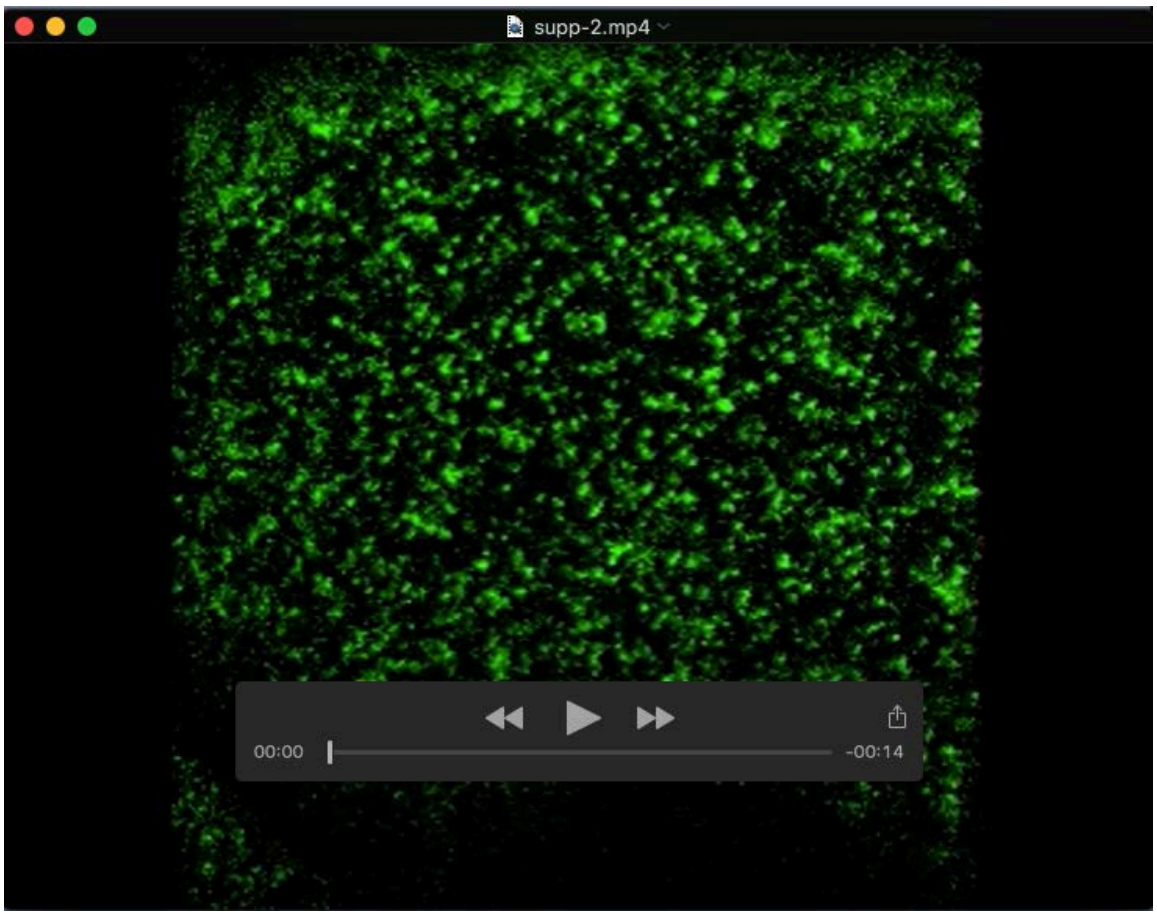

Movie S2. VA-TIRFM imaging of FLS2-GFP spots at the PM of *Arabidopsis* leaves epidermal cells after flg22 treatment. Movies of 100 frames were acquired; exposure time for each frame was 100 ms.

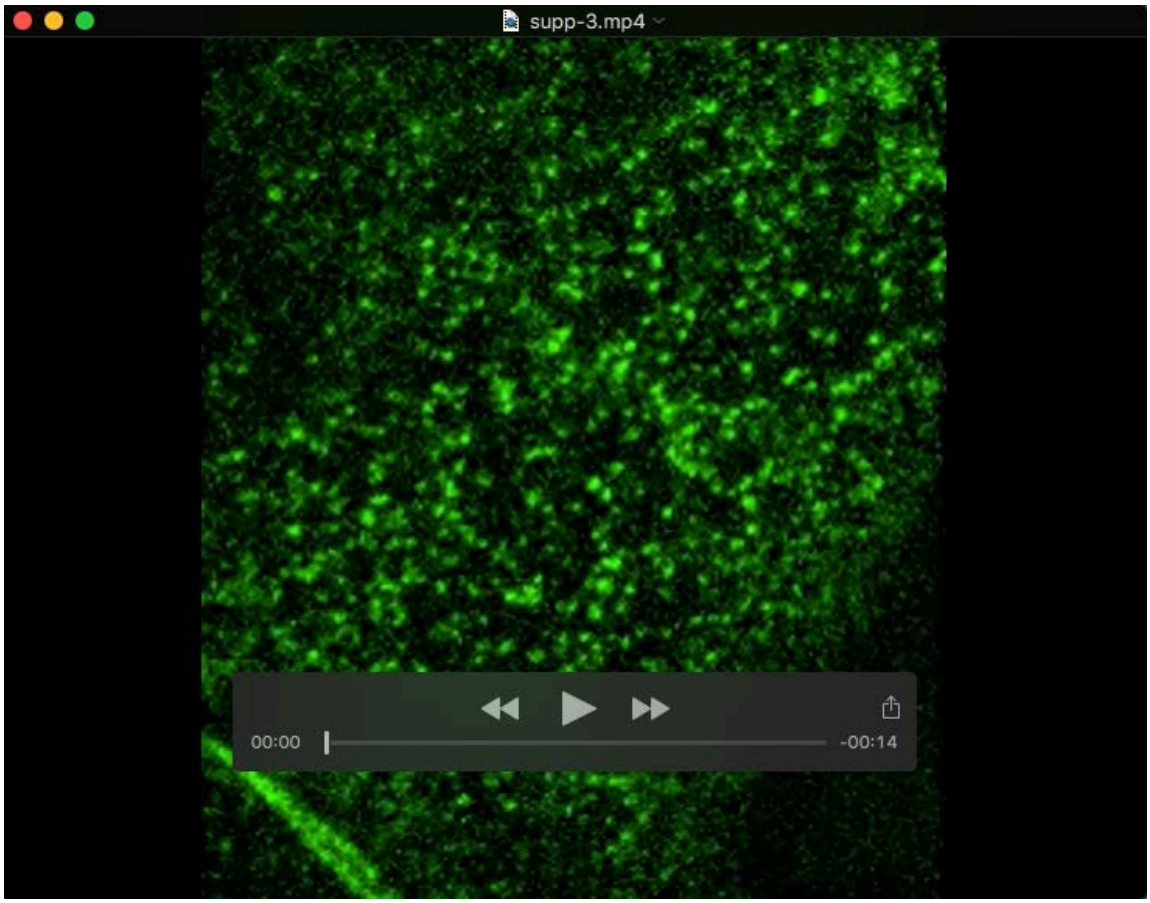

Movie S3. VA-TIRFM imaging of FLS2-GFP spots in *pFLS2*:FLS2-GFP transgenic seedlings in the *smt1* background. Movies of 100 frames were acquired; exposure time for each frame was 100 ms.

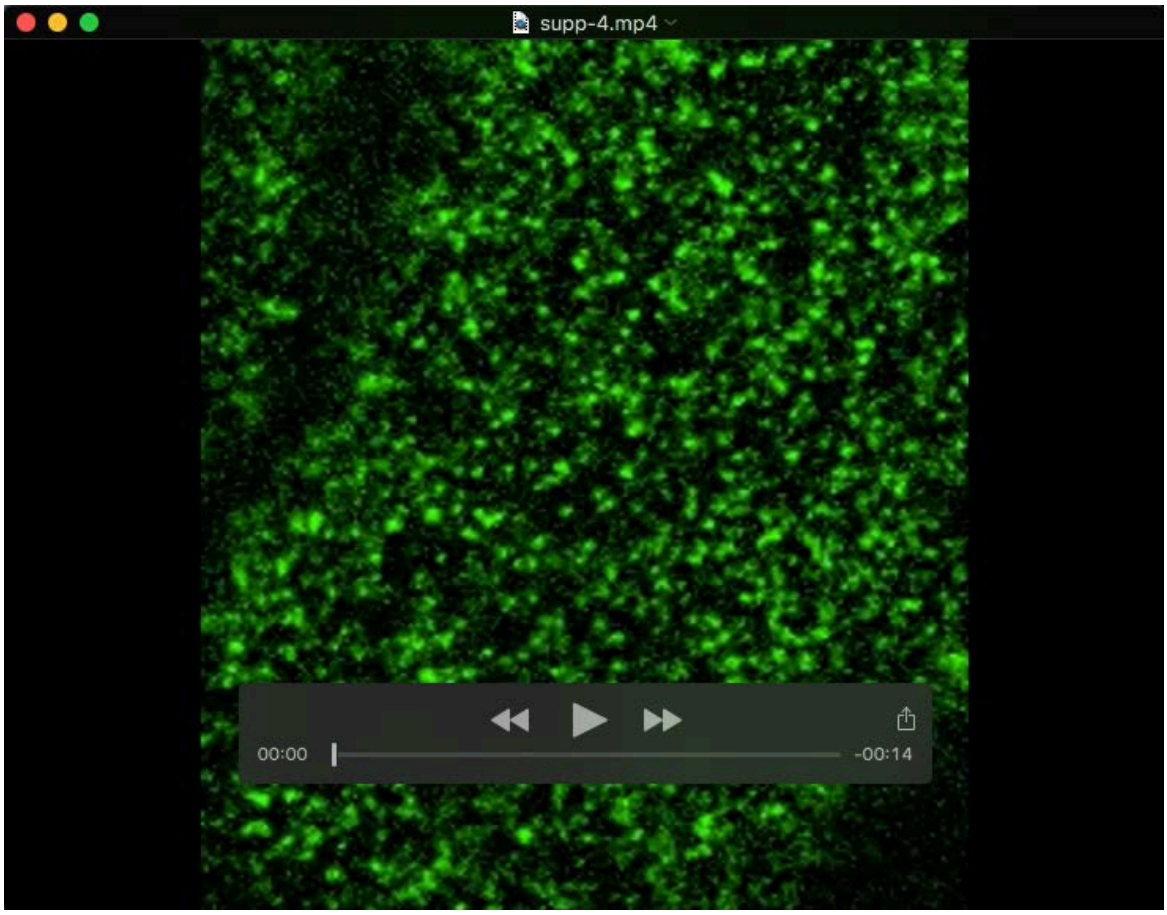

Movie S4. VA-TIRFM imaging of FLS2-GFP spots in *Arabidopsis* leaves epidermal cells treated with 10 mM MβCD. Movies of 100 frames were acquired; exposure time for each frame was 100 ms.